10-5-2017

# Failure Mechanisms of the Protective Coatings for the Hot Stamping Applications

Chen Zhao
*University of Windsor*

# Failure Mechanisms of the Protective Coatings for the Hot Stamping Applications

By

Chen Zhao

A Thesis

Submitted to the Faculty of Graduate Studies

Through the Department of Mechanical, Automotive and Materials Engineering

In Partial Fulfillment of the Requirements for

The Degree of Master of Applied Science

At the University of Windsor

Windsor, Ontario, Canada

2017

# Failure Mechanisms of the Protective Coatings for the Hot Stamping Applications

by

**Chen Zhao**

APPROVED BY:

_____

C. Chen

Department of Electrical and Computer Engineering

_____

V. Stoilov

Department of Mechanical, Automotive and Materials Engineering

_____

X. Nie, Advisor

Department of Mechanical, Automotive and Materials Engineering

August 15, 2017

# DECLARATION OF ORIGINALITY

I hereby certify that I am the sole author of this thesis and that no part of this thesis has been published or submitted for publication.

I certify that, to the best of my knowledge, my thesis does not infringe upon anyone's copyright nor violate any proprietary rights and that any ideas, techniques, quotations, or any other material from the work of other people included in my thesis, published or otherwise, are fully acknowledged in accordance with the standard referencing practices. Furthermore, to the extent that I have included copyrighted material that surpasses the bounds of fair dealing within the meaning of the Canada Copyright Act, I certify that I have obtained a written permission from the copyright owner(s) to include such material(s) in my thesis and have included copies of such copyright clearances to my appendix.

I declare that this is a true copy of my thesis, including any final revisions, as approved by my thesis committee and the Graduate Studies office, and that this thesis has not been submitted for a higher degree to any other University or Institution.

# ABSTRACT

In the present study, four different nitriding techniques were carried on the ductile irons NAAMS-D6510 and cast steels NAAMS-S0050A, which are widely used stamping die materials; duplex treatments (PVD CrN coating+nitriding) were carried on H13 steels, which are common inserts for the hot stamping dies.

Inclined impact-sliding wear tests were performed on the nitriding cases under simulated stamping conditions. Surface profilometer, scanning electron microscopy (SEM), energy-dispersive X-ray spectroscopy (EDS) and X-ray photoelectron spectroscopy (XPS) were used to investigate the wear and failure mechanisms of the protective coatings. It was found that the nitrided ductile iron samples performed better than the nitrided cast steel specimens. High temperature inclined impact-sliding wear tests were carried out on the CrN coatings. It was found that the coating performed better at elevated temperature. XPS analysis indicated the top surface layer (about 3-4nm) of the coating was oxidized at 400°C and formed a $Cr_2O_3$ protective film. The in-situ formation of the thin $Cr_2O_3$ protective layer likely led to the change of wear mechanisms from severe adhesive failure to mild abrasive wear.

# DEDICATION

To My Parents,

Xiaogan Zhao and Xueyun Wu

For their endless love and devotion

# ACKNOWLEDGEMENT

Sincere thanks have to be expressed to Dr. Xueyuan Nie, for providing me with the opportunity to work on this project under his excellent supervision. I am grateful to him for his great encouragement and endless support for the research.

I would like to thank the members of my committee Dr. Chunhong Chen and Dr. Vesselin Stoilov for their invaluable discussions, suggestions and time that helped to improve the final copy of this thesis. I would also like to acknowledge Dr. Mark Biesinger for the XPS analysis.

Sincere thanks are extended to the group members, Mr. Guang Wang and Mr. Rui Wang for their help and advice. Thanks also to everyone in the MAME Department who has offered me encouragement and support during the course of my study.

# TABLE OF CONTENTS

# LIST OF ABBREVIATIONS AND SYMBOLS

| | |
|---|---|
| AHSS | Advanced high-strength steel |
| CVD | Chemical vapor deposition |
| EDS | Energy-dispersive X-ray spectroscopy |
| POD | Pin-on-disk sliding wear test |
| PVD | Physical vapor deposition |
| SEM | Scanning electron microscopy |
| XPS | X-ray photoelectron spectroscopy |
| YS | Yield strength |
| UTS | Ultimate tensile strength |
| $V_w$ | Wear volume loss |
| $S_i$ | Section area of the *i*-th measurements along the wear track |
| $W_R$ | Wear rate |
| $E_s$ | Total sliding energy |

# LIST OF TABLES

# LIST OF FIGURES

# Chapter 1: Introduction

## 1.1 Motivation

In recent years, the use of advanced high-strength steels (AHSS) as structural reinforcements and in energy-absorbing systems in the automotive industry has increased rapidly; mainly given their favorable strength to weight ratios. However, due to the further increase in their high strength, the formability of AHSS is becoming poor at room temperature. Thus complex-shaped AHSS components are invariably produced through the hot metal forming processes. The use of hot stamping or press hardening, which was developed during the 1970's in northern Sweden [1], has become increasingly popular for the production of AHSS components, because of its reasonably high productivity and low cost. The number of produced parts increased from 3 million parts/year in 1987 to 8 million parts/year in 1997. Since the year 2000 more hot stamped parts have been used in the cars and the number of produced parts/year has gone up to approximately 107 million parts/year in 2007 [2].

Numerous researches have been carried on the formability of the AHSS and the optimization of the processing parameters [3-13]. Only very few papers have been published on the wear of the stamping dies [14, 15]. The elevated temperatures and high contact stresses enlarge the wear of the dies. Thus, understanding the wear and failure mechanisms of stamping dies with effects of both mechanical loads and temperatures is very important for the industry to improve the productivity and reduce the cost of equipment maintenance.

Protective coatings are considered as one of the best solutions to enhance the lifetime of the stamping dies, which do not alter the materials and designs. There are two different hot-stamping processes: the direct process and the indirect process. Nitriding can be used for the surface

modification of most working surfaces on the stamping dies where the stress levels are relatively low, while the duplex treatment, i.e. nitriding (with absence of white layer) plus physical vapor deposition (PVD) coating, can be applied to the forming, and flanging details of the stamping dies for surface protection against higher stress and elevated temperatures [16]. This duplex treatment is usually done by the "inserts" method.

To characterize the coating performance, there are various test methods. For instance, there are 838 active ASTM standards on coating properties and measurements, plus 585 existing ASTM standards on test procedures of coatings. Among this huge collection of coating characterization methods, these standards for friction and tribological evaluation include pin-on-disk, scratch, indentation or impacting. However, these conventional methods are deficient in evaluating coatings under stamping die working condition, where both impacting and sliding are involved simultaneously.

In this study, an inclined impact-sliding wear tester (which could provide both impacting and sliding simultaneously) was utilized to investigate the wear behaviors comprehensively, and failure mechanisms of different hot stamping die materials under extremely high contact stress. Two of the materials used in this project are nitrided cast iron NAAMS-D6510 and cast steel NAAMS-S0050A, which are the most used hot stamping die materials. Another material tested in the present study is the H13 steel with duplex treatment (PVD CrN coating + plasma nitriding), which is a popular insert for the hot stamping die to enhance the forming and flanging details. After the wear tests, the samples were examined by a surface profilometer, scanning electron microscope (SEM), energy-dispersive X-ray spectroscopy (EDS), and X-ray photoelectron spectroscopy (XPS) to figure out the wear behaviors and failure mechanisms.

## 1.2 Objectives of this study

The objectives of this study are to:

1) Develop a high-temperature inclined impact-sliding wear testing method and figure out the suitable test conditions;
2) Investigate the wear behaviors and failure modes of stamping die materials (ductile cast iron and steel) with different surface treatments under simulated stamping condition;
3) Investigate the wear behaviors and failure modes of the inserts for the stamping die (H13 steel with duplex treatment) at both room temperature and elevated temperatures.

## 1.3 Organization of the Thesis

This thesis includes six chapters. In chapter 1, motivation of the research is introduced; the research was mainly investigating into effects of surface modification techniques on wear behaviors of stamping die materials.

Chapter 2 gives the literature review of hot stamping processes, surface modification technologies and the characteristics of different types of coatings. The tribological investigation on the nitrided irons and steels as well as PVD CrN coatings are also reviewed.

Chapter 3 describes the test facilities, experimental procedures, and characterization instrumentation. Chapters 4 and 5 summarized the test results of the die materials (nitrided irons and steels) and the inserts (H13 steel with duplex treatment) of the hot stamping die, respectively. For the conclusions and future works, Chapter 6 gives a detailed summary.

# Chapter 2: Literature review

## 2.1 Advanced high strength steel applications in automotive industry

As automotive industries are challenged to improve the safety and fuel economy, they search for new materials to meet higher standards. Materials in the motor applications are selected to minimize weight while meeting key criteria including formability, crash performance, and stiffness. Different types of advanced high strength steels help parts meet the varied performance demands in various areas of the vehicle, including both the crumple zone and passenger compartment [16].

Advanced high strength steels are a newer generation of steel grades that provide extremely high strength while maintaining the high formability required for manufacturing, which could help engineers meet the safety requirements, emission limits, productivity, durability, and quality at an acceptable cost [17]. A typical definition calls steels with 210 to 550 MPa yield strength "high strength" and anything stronger "advanced high strength." AHSS steels are also sometimes called "ultra-high strength steels" for tensile strengths exceeding 780 MPa [18]. AHSS with a tensile strength of at least 1000 MPa is often called "GigaPascal steel" (1000 MPa =1GPa) [18].

The AHSS can be classified as the following types: dual phase, complex phase, ferritic-bainitic, martensitic, transformation-induced plasticity, hot-formed, and twinning-induced plasticity steels. The generic classification method was developed by FutureSteelVehicle (FSV) [19], in which the steels are identified as XX aaa/bbb where XX is the type of steel while aaa and bbb are the minimum yield strength (YS) and ultimate tensile strength (UTS), respectively. Each has unique microstructural features, alloying additions, processing requirements, advantages and

challenges associated with its use. Each type has unique applications where it might be best employed to meet performance demands of the part.

Dual phase steels are currently the most widely used AHSS. In 2010, the Auto/Steel Partnership published “Advanced high-strength steel applications: Design and stamping process guidelines,” a special edition with 12 in-depth AHSS case studies [20]. Most of the parts in this report were produced from DP steel. Details from part geometry design, stamping process design, formability analysis, die process, spring back compensation, press load predictions, fixture, and clamping are noted, as well as lessons learned from the study. Automakers increasingly use DP in current car models. For example, in the 2011 Chevrolet Volt, the overall upper body structure is six percent DP by mass, and the lower structure is 15 percent, including such parts as the reinforcement for the rocker outer panel [21].

The future of AHSS for automotive applications is bright. Many groups are researching these new steels to understand their properties better and to continue tailoring unique sets of characteristics. Others are focused on improving the technologies necessary for manufacturing parts made of AHSS. The steel and automotive industries have forged numerous partnerships to develop the materials and technologies necessary to put the next generation of safer and more environmentally friendly vehicles on the road.

### 2.2 Hot stamping for the AHSS

Due to the increase of their high strength, the formability of AHSS becomes poor at room temperature. Thus complex-shaped AHSS components are invariably produced through the hot metal forming processes. The use of hot stamping or press hardening, which was developed during the 1970’s in northern Sweden [1], has become increasingly popular for the production of

AHSS components, because of its high productivity and low cost. The number of produced parts increased from 3 million parts/year in 1987 to 8 million parts/year in 1997. Since the year 2000 more hot stamped parts have been used in the cars and the number of produced parts/year has gone up to approximately 107 million parts/year in 2007 [2].

### 2.2.1 Processes of the hot stamping

As shown in Figure 2.1 [22], there are two different hot stamping processes:

1) Indirect process: the blank is formed, trimmed, and pierced in cold condition. It is later heated and quenched in a die to get high strength properties;
2) Direct process: the unformed blank is heated in a furnace, formed in hot condition, and quenched in the die to achieve the required properties.

Selection of the process depends on the part complexity and the blank coating (Zn-based coatings typically require the indirect process). In either method, the blank is formed in a much softer and formable state and is later hardened in the dies, which have drilled cooling channels.

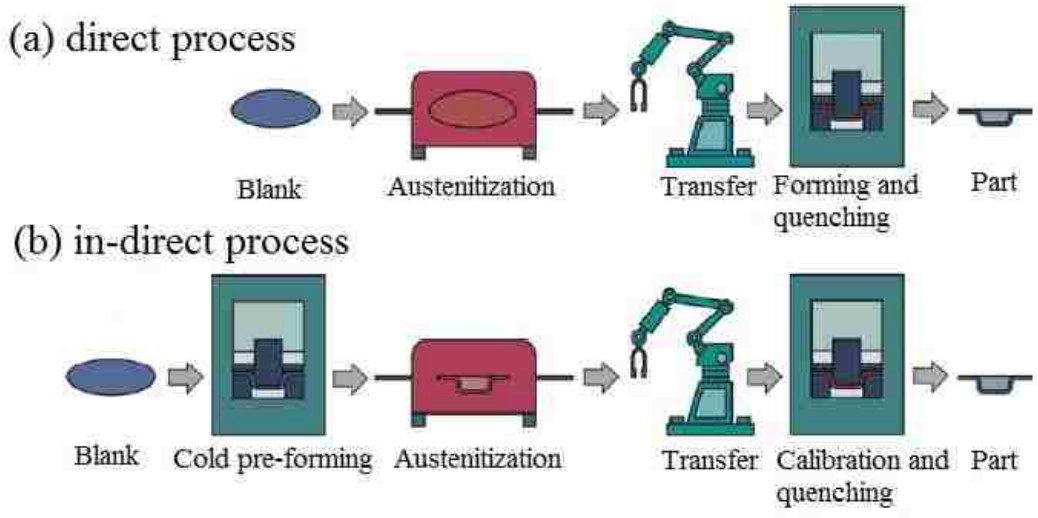


Figure 2.1 Setup illustration of the (a) direct; and (b) indirect hot stamping processes [22].

Three main procedures control the hot stamping: heating, forming and quenching. Numerous researches have been published in these areas.

The investigations of Lechler [23] have shown that the heating procedure of the blank has a significant influence on the part properties, the process time, and the cost-efficiency of hot stamping. Therefore, a homogeneous blank temperature and a short heating time are the main demand on the heating system. The blank can be heated using different thermal phenomena: radiation in a furnace [24, 25], induction [26, 27], and conduction [28, 29].

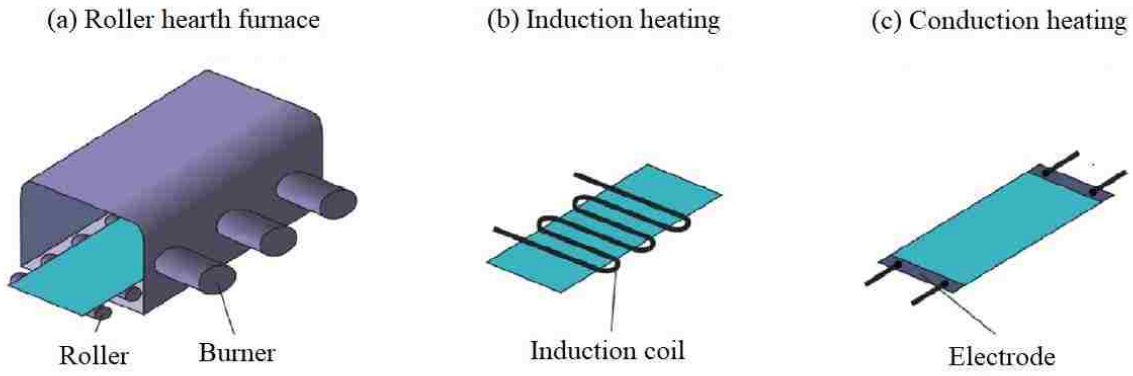


Figure 2.2 Setup illustration of the (a) radiation; (b) induction; and (c) conduction heating methods for the hot stamping process [30].

The blank must be transferred as quickly as possible from the furnace to the press to minimize the cooling of the part before forming. Furthermore, forming must be completed in a much softer and formable state, which is before the beginning of the martensite transformation. Therefore, a fast tool closing and forming process are the precondition for a successful process control. After forming, the part is quenched in the closed tool, which is cooled by water ducts to transfer the heat out of the tool system. To avoid the quenching of the blank between the blank

holder and the die during the forming process, most of the hot stamping tool systems work with a distance blank holder.

### 2.2.2 Materials for the hot stamping

The investigations on ultra-high strength steels by Naderi [31] have shown that boron alloys of 22MnB5, 27MnCrB5, and 37MnB4 steel grades (Table 2.1) are the only steel grades which produce a fully martensitic microstructure after hot stamping when a water-cooled stamping die is used. Among them, 22MnB5 steel grade is the most commonly used steel grade in hot stamping processes. Initially, the material exhibits a ferritic-pearlitic microstructure with a tensile strength of about 600 MPa. After the hot stamping process, the component finally has a martensitic microstructure with a total strength of about 1500MPa. During the quenching inside the die, if the cooling rate exceeds a minimum cooling rate of approximately 27 K/s, at a temperature of around 400˚C, a diffusionless martensitic transformation will be induced (Figure 2.3), which finally is responsible for the resulting high strength of the part [32].

Table 2.1 Chemical components and mechanical properties of boron steels [31].

| Steel | Al | B | C | Cr | Mn |
|---|---|---|---|---|---|
| 20MnB5 | 0.04 | 0.001 | 0.16 | 0.23 | 1.05 |
| 22MnB5 | 0.03 | 0.002 | 0.23 | 0.16 | 1.18 |
| 8MnCrB3 | 0.05 | 0.002 | 0.07 | 0.37 | 0.75 |
| 27MnCrB5 | 0.03 | 0.002 | 0.25 | 0.34 | 1.24 |
| 37MnB4 | 0.03 | 0.001 | 0.33 | 0.19 | 0.81 |

| Steel | N | Ni | Si | Ti |
|---|---|---|---|---|
| 20MnB5 | 0 | 0.01 | 0.4 | 0.034 |
| 22MnB5 | 0.005 | 0.12 | 0.22 | 0.04 |
| 8MnCrB3 | 0.006 | 0.01 | 0.21 | 0.042 |
| 27MnCrB5 | 0.004 | 0.01 | 0.21 | 0.042 |
| 37MnB4 | 0.006 | 0.02 | 0.31 | 0.046 |

| Steel | Martensite start temperature (˚C) | Critical cooling (K/s) |
|---|---|---|
| 20MnB5 | 450 | 30 |
| 22MnB5 | 410 | 27 |
| 8MnCrB3 | * | * |
| 27MnCrB5 | 400 | 20 |
| 37MnB4 | 350 | 14 |

| Steel | Yield stress (MPa) | | Tensile strength (MPa) | |
|---|---|---|---|---|
| | As delivered | Hot stamped | As delivered | Hot stamped |
| 20MnB5 | 505 | 967 | 637 | 1354 |
| 22MnB5 | 457 | 1010 | 608 | 1478 |
| 8MnCrB3 | 447 | 751 | 520 | 882 |
| 27MnCrB5 | 478 | 1097 | 638 | 1611 |
| 37MnB4 | 580 | 1378 | 810 | 2040 |

* There is no possibility to have fully martensitic microstructure.

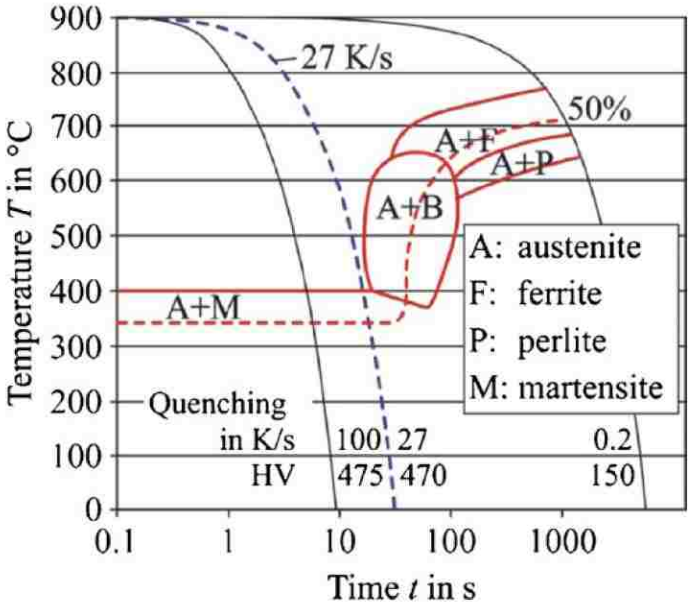


Figure 2.3 CCT diagram of 22MnB5, showing the martensitic transformation at a temperature of around 400˚C with a minimum cooling rate of 27K/s [32].

### 2.3 Surface modifications of the hot stamping dies

The elevated temperatures and high contact stresses enlarge the wear of the dies. Meanwhile, the building cost of the hot stamping dies continuously increases. Therefore, the automotive industries desire to extend the lifespan and reduce the maintenance cost of the stamping dies. Protective coatings seem to be the best solution to enhance the lifetime of the stamping dies, which do not alter the materials and designs.

Nitriding can be used for the surface modification of the less-stressed surface areas of the stamping dies at lower temperatures (this is the case for the most surface areas of the dies) Meanwhile, duplex treatment, i.e. nitriding (with absence of white layer) plus physical vapor deposition (PVD) coating, can be applied for enhancing the forming and flanging details of the

direct hot stamping dies for surface protection at elevated temperatures [16]. This duplex treatment is usually accomplished by the “inserts” method.

### 2.3.1 Surface modification technologies

Depending on applications and cost efficiency, protective coatings can be applied to the parts by different approaches or the combination of different surface treatments [33-39]. For example, deposition (TiN, CrN, and TiAlN by PVD) on the surface of modified substrate (plasma nitriding/nitrocarburizing), which is usually called duplex treatment, has been widely used to improve the wear and scuffing resistance, as shown in Figure 2.4 [40]. This combination results in high wear resistance, high strength, and high load capacity. These superior properties are due to an increase of substrate hardness, fatigue strength. The wear/corrosion resistance offered by the hard PVD coatings and a more gentle transition of elastic-plastic properties between the outermost layer of the coating and the substrate, as shown in Figure 2.5 [41], also contribute to the improved performance of duplex treatment.

Although coating techniques are various, plasma nitriding/nitrocarburizing, thermal spray, CVD and PVD coatings are the most commercially available ones and will be explained in detail.

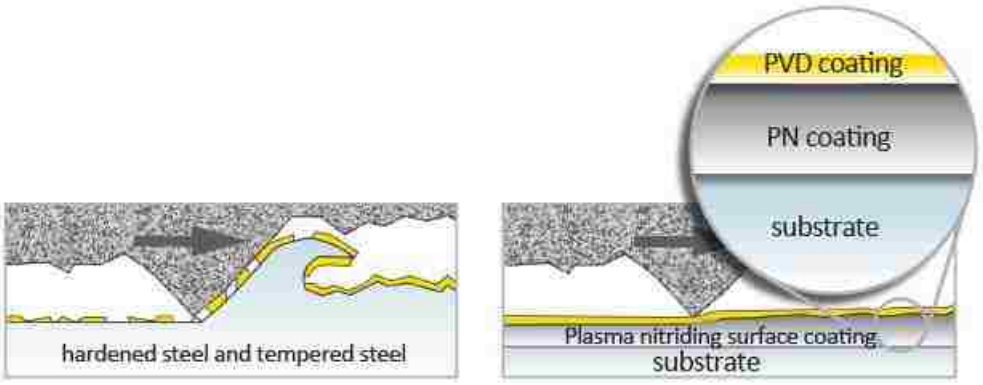


Figure 2.4 Schematic drawing of the hardened steel and duplex treatment, showing the superior wear and scuffing resistance of the duplex treatment [40].

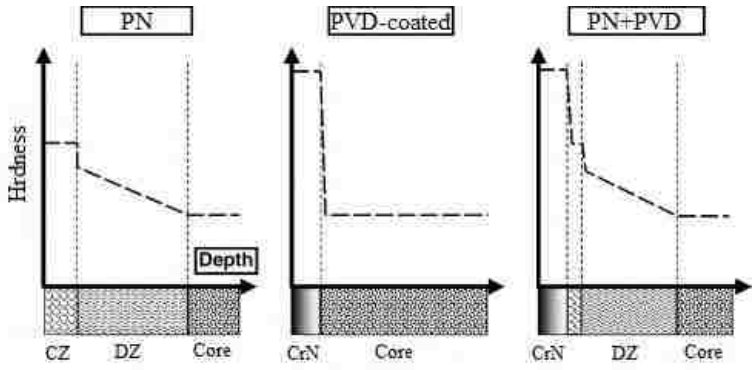


Figure 2.5 Hardness versus distance from the surface for soft steels with a plasma nitriding treatment (PN), PVD coating, and combination nitriding plus PVD coating; CZ: compound zone, DZ: diffusion zone [41].

#### *2.3.1.1 Plasma nitriding/nitrocarburizing*

In plasma nitriding, the reactivity of the nitriding media is not due to the temperature but to the gas ionized state. In this technique, intense electric fields are used to generate ionized molecules of the gas around the surface to be nitrided. Such highly active gas with ionized molecules is called plasma, naming the technique. The gas used for plasma nitriding is usually pure nitrogen since no natural decomposition is needed (as is the case of gas nitriding with ammonia). There are hot plasmas typified by plasma jets used for metal cutting, welding,

cladding or spraying. There are also cold plasmas, usually generated inside vacuum chambers, at low-pressure regimes [42]. Figure 2.6 shows a schematic illustration of the plasma-nitriding reactor.

Plasma nitriding permits the close control of the nitrided microstructure, allowing nitriding with or without the white layer formation. By carefully choosing the process parameters, a higher surface hardness, lower friction coefficient compared to the untreated materials, and a compressive residue stress in the nitriding case could be achieved with relatively limited distortion and dimensional variation [42]. Therefore, no machining, polishing or any other post-nitriding operations are needed; the process is user-friendly, energy saving and of high productivity.

Moreover, since nitrogen ions are made available by ionization, differently from gas or salt bath nitriding, plasma nitriding efficiency does not depend on the temperature. Plasma nitriding can thus be carried out in a broad temperature range, from 260°C to more than 600°C [43]. For instance, at moderate temperatures (like 420°C), stainless steels can be nitrided without the formation of chromium nitride precipitates and hence maintaining their corrosion resistance properties.

The main shortcoming of this process is that the surface hardness of nitrided materials is not as high as that of the very hard PVD coatings. Therefore, plasma nitriding is often coupled with PVD process and labeled as Duplex Treatment, with enhanced benefits. Many users also prefer to have a plasma oxidation step as the last phase of processing to produce a smooth layer of oxides which is resistant to wear and corrosion.

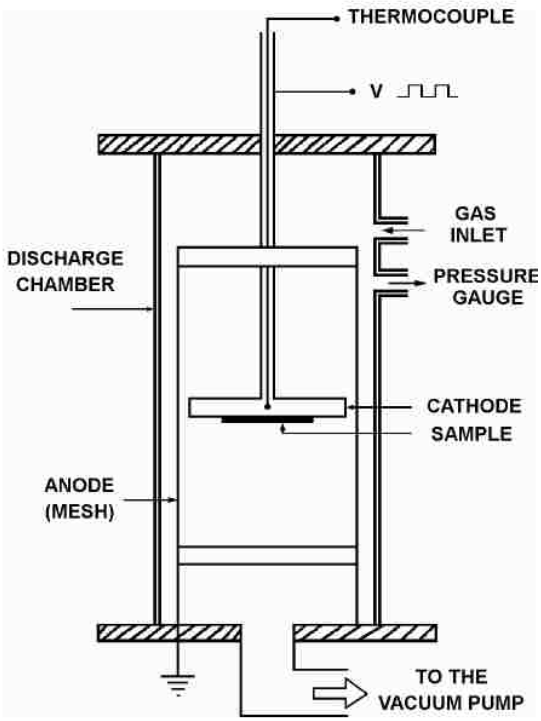


Figure 2.6 A schematic illustration of the plasma-nitriding reactor [42].

### *2.3.1.2 Thermal spray*

Thermal spray coatings are deposited by impacting molten, semi-molten or solid particles of various materials on the substrates. The thickness pf thermal spray coatings could vary from a few micrometers to several millimeters [44]. Figure 2.7 shows the schematic illustration of the thermal spray facility and typical microstructure of thermal spray coatings.

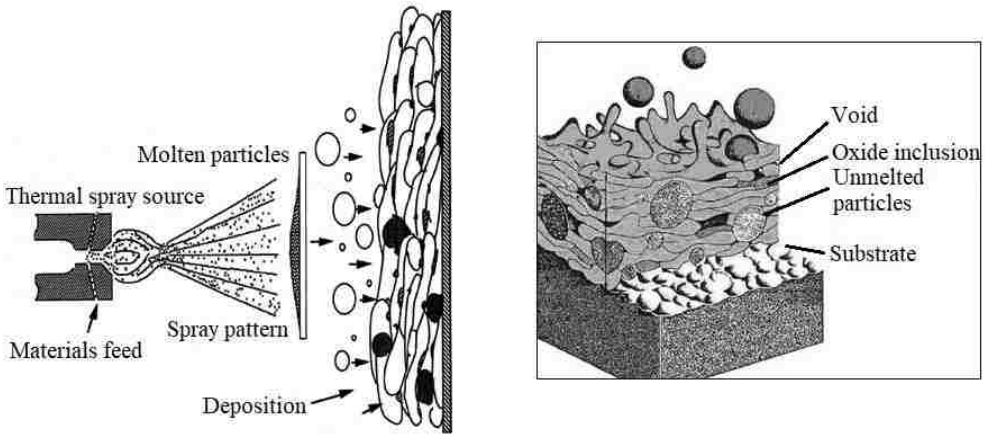


Figure 2.7 Schematic illustration of (a) thermal spray process [44], (b) typical microstructure of thermal spray coating [45].

There are several advantages of thermal spray process such as:

a) A wide range of materials including metals, alloys, carbides, oxides, non-oxide ceramics and any combinations of these could be used for thermal spray coatings;

b) The deposition rate of thermal spray process is higher than that of PVD or CVD processes with minimal requirement for base materials preparation;

c) The lower processing temperature of the substrate and thus minimal thermal degradation to the substrate.

However, the unmolten particles, voids, cracks and the incomplete bonding lead to an uneven microstructure of the coating and decrease its thermal conductivity, strength and load capacity [45]. The main shortcomings of thermal spray coatings are low strength, porosity, anisotropic, low loading capacity and line-of-sight process, which means it is difficult to apply coatings to complex shapes. Therefore, the thermal spray coatings are suitable for thermal barrier function rather than load bearing.

#### *2.3.1.3 Vapor deposition technologies*

Compared to thermal spray coatings, vapor deposition coatings have the much high bond strength (minimum tensile strength 103 MPa using ASTM 633) than thermal spray coatings which have a range from 41 to 83 MPa [45]. Other advantages of vapor deposition techniques include controllable microstructure, extremely high surface hardness, enhanced fatigue toughness, high wear and corrosion resistance. All these benefits make vapor deposition coatings much more suitable for load bearing function than thermal spray coatings. Figures 2.8 and 2.9 show the typical PVD and CVD techniques, respectively. In PVD, a pure source material is gasified via evaporation, the application of high power electricity, laser ablation, and a few other techniques. The gasified material will then condense on the substrate material to create the desired layer. There are no chemical reactions that take place in the entire process. Depending on the methods for gasifying and transporting, it can be divided into sputter deposition, cathodic arc, ion plating and ion beam-assisted deposition (IBAD) [46]. In CVD, the source material is not pure as it is mixed with a gaseous precursor that acts as a carrier. The mixture is injected into the chamber that contains the substrate and is then deposited into it. When the mixture already adheres to the substrate, the precursor eventually decomposes and leaves the desired layer of the source material in the substrate. The by-product is then removed from the chamber via gas flow. The process of decomposition can be assisted or accelerated via the use of heat, plasma, or other processes [47].

Vapor deposition technologies also have their advantages and disadvantages. For instance, the main benefit of CVD over PVD is that CVD is not a line-in-sight process and thus can deal with relatively complex shapes. Other advantages of CVD process include higher deposition rate, large thickness than can be achieved plus relatively simple equipment without high vacuum like

PVD. However, CVD process is far from a universal technique. Firstly, the substrate must be heated up to around 600°C or higher to initiate the chemical reaction at the sample surface, and post heat treatment may be required for steel working piece, leading to a thermal induced distortion and dimensional variation. This means that CVD process is not suitable for precision metal parts. Moreover, some precursors and by-products are toxic and corrosive which require careful consideration of disposal processing and incur additional costs. On the contrary, PVD process involves direct deposition of coating materials on the prepared surfaces; no chemical reaction is required which means there is no by-products or pollutants. Therefore, the process can work at a wide range of temperatures, and there is no need to heat up the substrate, which means PVD process can deal with precision metal parts and no post heat treatment is required. The raw materials of PVD process include metals, alloys, and ceramics. PVD process can deposit unique microstructure such as amorphous with high bond strength and fine surface finish. However, PVD process also has some drawbacks. Firstly, PVD is a line-in-sight process and thus applying PVD coatings on complex surfaces can be a big challenge. Secondly, PVD process requires high vacuum which increases the complexity and cost of the process. Moreover, the significant mismatch of elastic-plastic properties at the boundary between PVD coating and substrate surface usually leads to severe coating failure such as cracking and delamination when subjected to high pressures [41]. To solve this problem, PVD process is usually combined with plasma nitriding/nitrocarburizing to get a gentle transition of elastic-plastic properties between the outermost layer of the coating and the substrate. This kind of treatments is called duplex treatment.

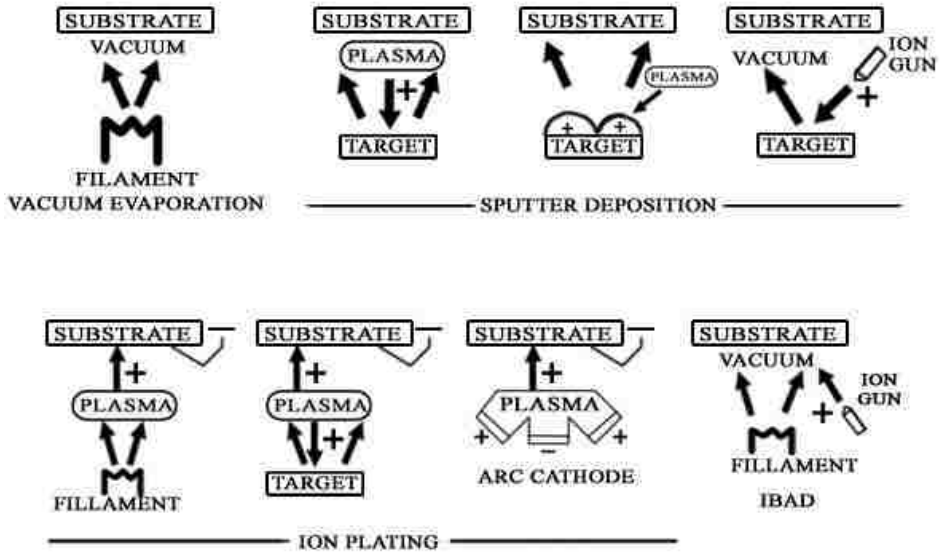


Figure 2.8 PVD processing techniques include vacuum evaporation, sputter deposition, ion plating and ion beam assisted deposition (IBAD) [46].

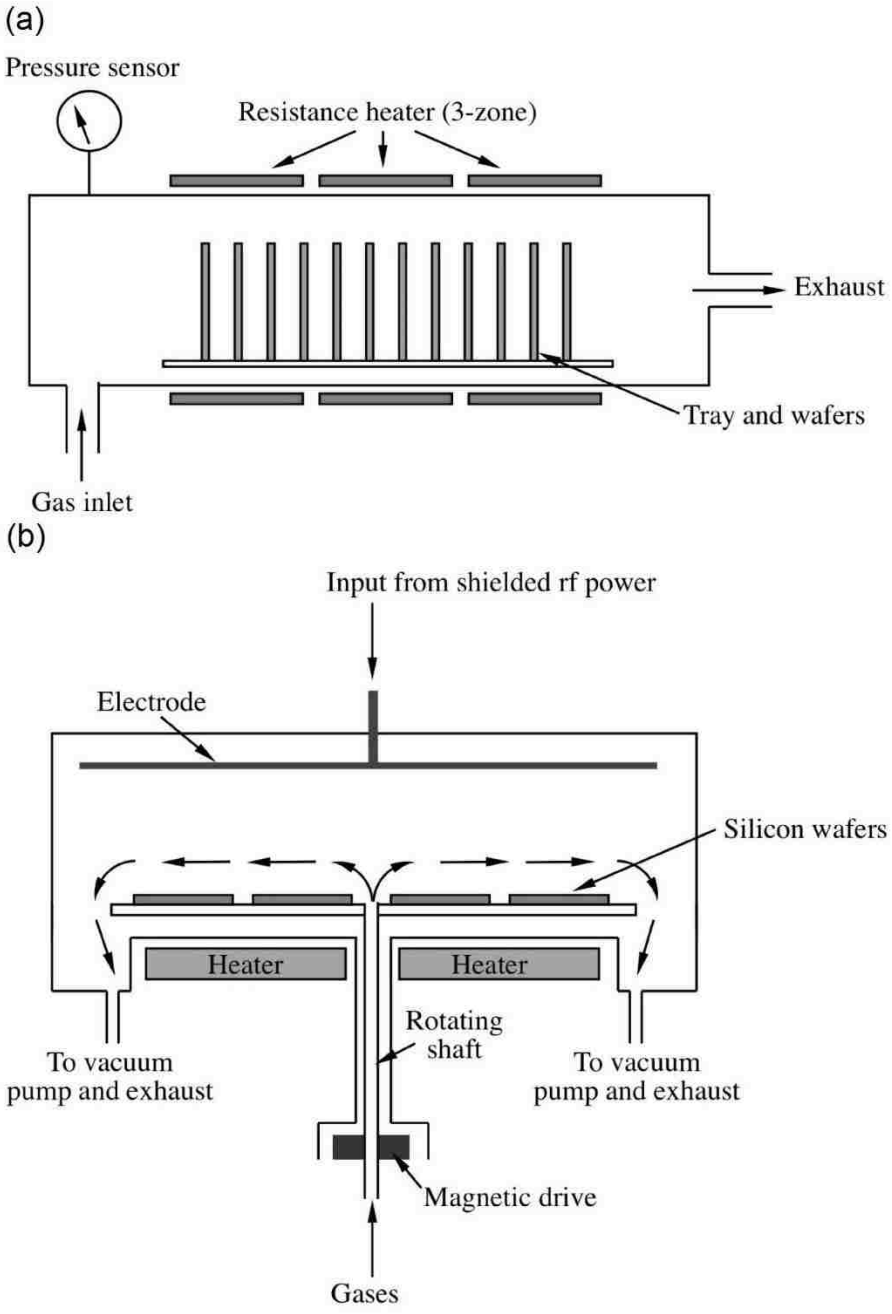


Figure 2.9 Schematic illustrations of (a) low pressure CVD (LPCVD) processing, (b) plasma enhanced CVD (PECVD) processing [47].

### 2.3.2 Tribological properties of the modified surfaces

As mentioned above, compared with plasma nitriding/nitrocarburizing and vapor deposition coatings (CVD and PVD processing), thermal spray coating are not suitable for load bearing or tribological applications due to low hardness and low bonding strength. Therefore, in this section, we will only review the characterization of plasma nitriding/nitrocarburizing, physical vapor deposition (PVD processing) and duplex treatment coatings, CVD processing will be omitted due to its inherent drawbacks.

#### *2.3.2.1 Characterization of plasma nitriding/nitrocarburizing cases*

The tribological behaviors of plasma nitriding steels/irons during pin-on-disk sliding tests under dry conditions at room temperature have been extensively studied in recent years. It has been reported that the nitriding case consists of an outermost compound layer with a hardness of 800-1800 HV, varies with different processing parameters and substrate materials, and a diffusion zone with decreasing nitrogen concentration [48-50], as shown in Figure 2.10. The compressive residue stresses in the nitriding cases, as illustrated in figure 2.11, are reported to significantly improve the fatigue strength and wear resistance [50-53].

The reports of the influence of plasma nitriding on the friction coefficient under dry sliding conditions are not consistent and may rely on the substrate materials [48, 54 and 55], as shown in Table 2.2 and Figure 2.12. Nie et al. [54] reported that plasma nitriding increased the friction coefficient of cast iron G3500 while the influence of plasma nitriding on the friction coefficient on cast steel S0050A was minimal. Mehmet Karakan et al. [55] also reported that plasma nitriding increased the friction coefficient of AISI 4140 steel. On the other hand, Xi et al. [48] reported plasma nitriding significantly decreased the friction coefficient of AISI 420 stainless steel.

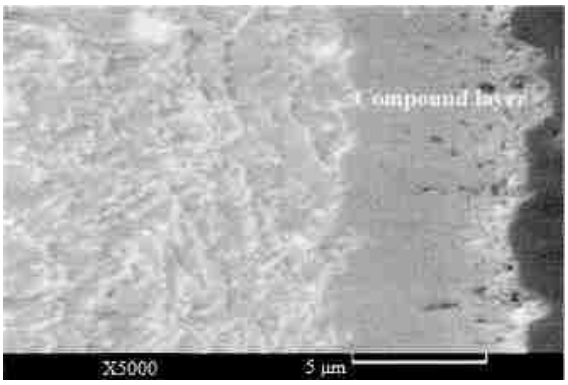


Figure 2.10 Micrograph of a cross-section of plasma nitrided AISI 4140 steel with a compound layer (nitrided in a 75%$H_2$–25%$N_2$ gas mixture) [49].

The actual influence of compound layer on the wear resistance of plasma nitrided steels/irons is still to be certified [49, 55, and 56]. Podgornik, B., et al. [49] claimed that the presence of a hard and brittle compound layer on the surface of plasma nitrided AISI 4140 steel caused an increased wear, which was due to the fracture of the compound layer and hard abrasive particle formation in the initial stage of sliding. While Mehmet Karakan et al. [55] reported, for plasma nitrided AISI 4140 steel, the wear resistance was improved according to untreated specimen due to the compound layer. As shown in Table 2.2, the samples treated for 4 hours with the thickest compound layer showed the lowest wear rate among all treated and untreated samples.

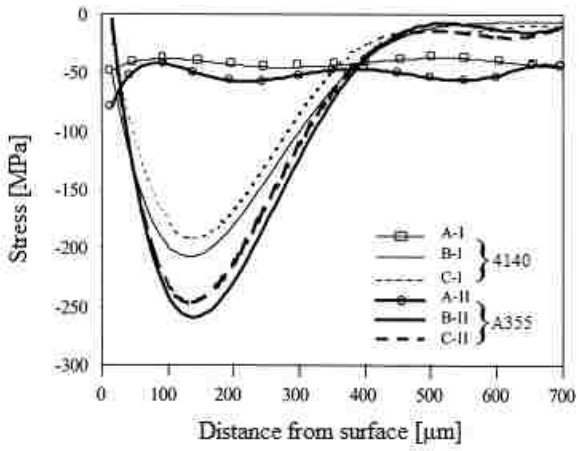


Figure 2.11 Residual stress distribution for different surface treatments and materials; I and II represent AISI 4140 steel (42CrMo4) and AISI A355 steel (34CrAlMo5), respectively; A, B, and C represent hardening, plasma nitriding, and pulsed plasma nitriding, respectively [50].

Despite the inconsistent reports about the friction coefficients of treated steels/irons and the effect of the white layer on the wear resistance of treated samples, most of the literature agree with that plasma nitriding/nitrocarburizing can significantly improve the wear resistance of steels/irons [48-58]. It has been reported that the wear of untreated steels/irons is characterized with severe adhesive wear, materials transfer, plastic deformation and fatigue failure [48, 54-58]. After plasma nitriding treatment, the wear is then characterized with mild abrasive wear, polishing of nitrided surfaces and oxidation wear [48-50, 52-58].

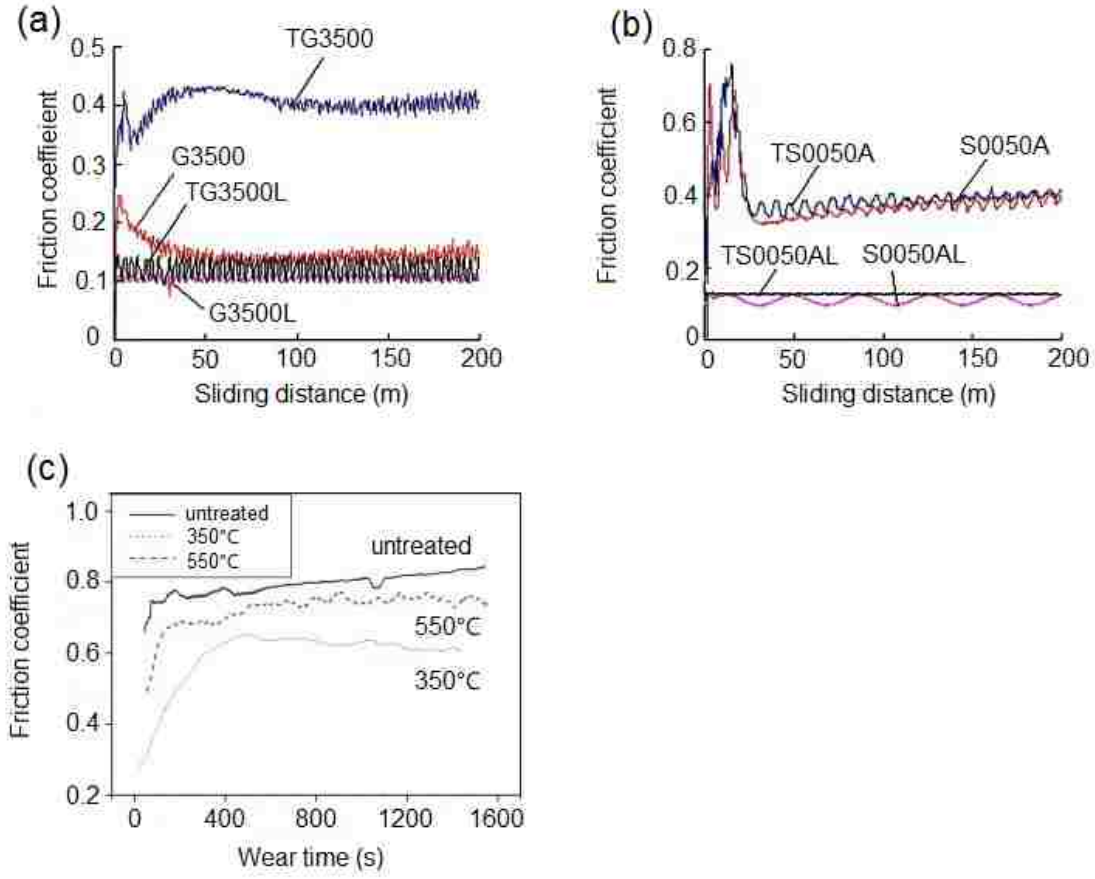


Figure 2.12 (a) Tribological behaviours without (with) lubricants of treated/untreated TG3500 (L)/G3500 (L) and TS0050A(L)/S0050A(L) samples [54]; (b) Friction coefficient of the untreated and nitrided AISI 420 steel samples [48].

Table 2.2 Structural and Tribological properties of ferritic plasma nitrocarburized AISI 4140 steel [55].

| Experimental results obtained after plasma nitrocarburizing at 570 °C | | | | | | | |
|---|---|---|---|---|---|---|---|
| Process parameters | | Structural properties | | Mechanical properties | | Tribological properties | |
| Temperature (°C) | Time (h) | Compound layer (μm) | Diffusion layer (μm) | Surface hardness (HV0.05) | Surface roughness (Ra) | Wear rate ($\times 10^{-6}$ $mm^3/Nm$) | Friction coefficient |
| 570 | 1 | 15-17 | 150-170 | 390-430 | 0.15-0.25 | 1.6-1.8 | 0.57-0.59 |
| | 2 | 16-18 | 180-200 | 410-450 | 0.15-0.25 | 1.5-1.7 | 0.59-0.61 |
| | 4 | 17-19 | 210-230 | 530-570 | 0.62-0.72 | 1.3-1.5 | 0.58-0.60 |
| | 8 | 15-17 | 260-280 | 510-550 | 0.68-0.78 | 1.4-1.6 | 0.59-0.61 |
| | 12 | 14-15.5 | 280-230 | 460-500 | 0.70-0.80 | 1.5-1.7 | 0.57-0.59 |
| | Untreated | NA | NA | 322 | 0-0.1 | 2.7-2.9 | 0.50-0.52 |

However, no literature has been published yet to investigate the wear behaviors and failure mechanisms of nitrided iron/steels under extremely high contact stresses involving impacting and sliding simultaneously.

#### *2.3.2.2 Characterization of TiN PVD Coating*

Among various kinds of PVD coatings, thin films of transition metal nitrides have been applied on surfaces of machine tools such as cutting tools and stamping dies due to their high hardness, excellent wear resistance, and chemical inertness. These benefits are attributed to the bond structure in transition metal nitrides, which consists of a mixture of covalent, metallic and ionic components [59].

Of the transition metal nitrides, processing techniques, properties, and applications of titanium nitride (TiN) have been extensively investigated [60-63]. Titanium nitride crystallizes in the B1 NaCl structure and exists a solid solution containing nitrogen in the range 37.5-50 at. % as shown in Figure 2.13 [59].

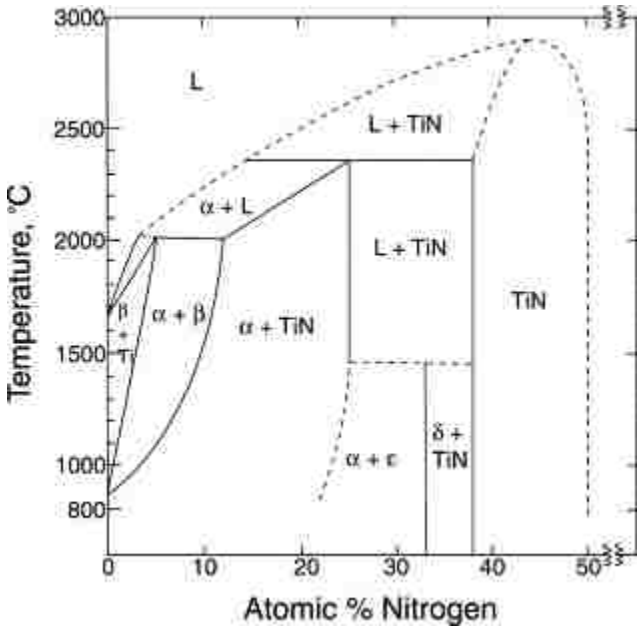


Figure 2.13 Equilibrium phase diagram of Ti-N binary system [59].

A. T. Alphas et al. [60] have studied the tribological behaviors of TiN PVD coatings over a range of contact loads (20–250 N) at a constant sliding speed of 0.7 m/s against AISI M2 high-speed steel pins in a pin-on-disk configuration. Three different wear regimes could be distinguished as shown in Figure 2.14 (a): (i) Transfer and build-up of oxidized pin debris on the coating surface accompanied by slight polishing damage of the TiN at the lowest applied load of 20 N, leading to negative mass loss of the coating system. (ii) Tests at loads of between 50 and 100 N showed increased polishing damage and brittle spallation failure of the TiN. Wear rates of the TiN coating showed a linear increase with a load in this regime and were combined with increased friction heating of the pin and a reduction in steady-state coefficient of friction, as

shown in Figures 2.14 (b) and (c). (iii) A sharp transition to a plastic deformation and micro plowing wear mechanism occurred at loads greater than 100 N and the attainment of a pin temperature of approximately 160°C.

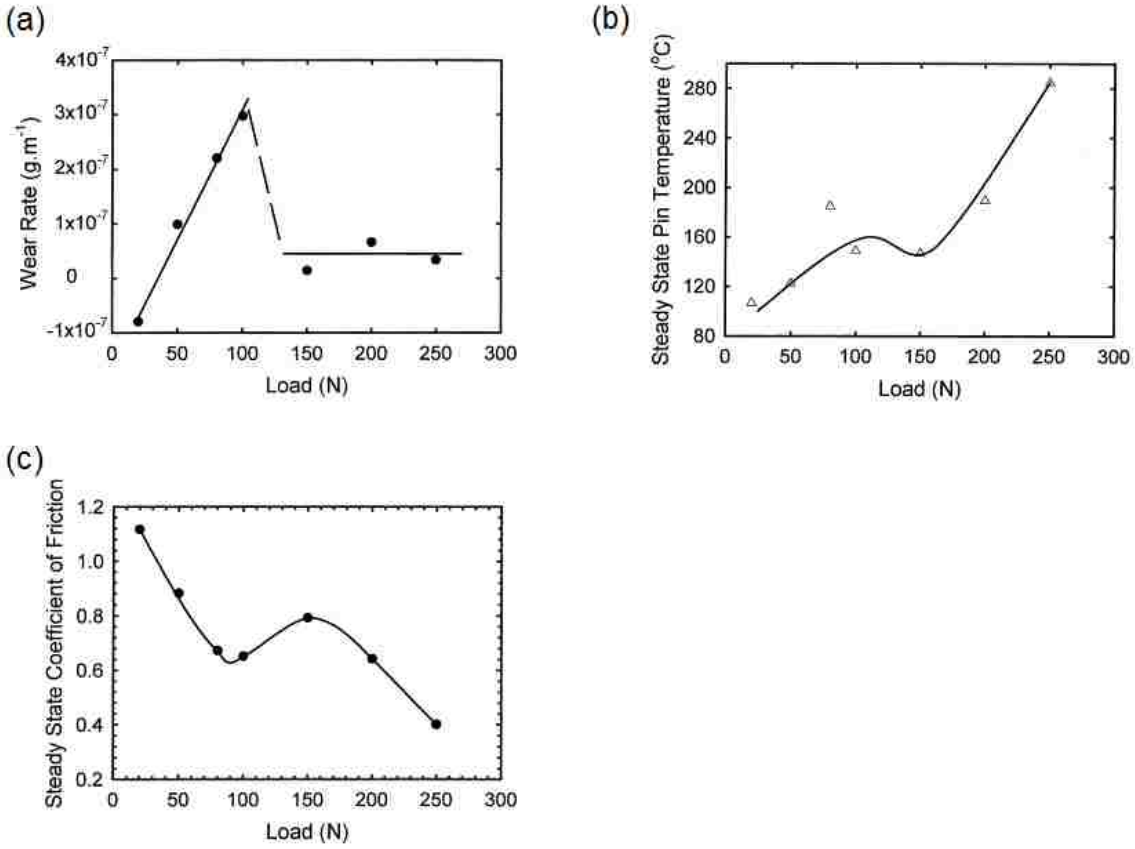


Figure 2.14 (a) Wear rate vs. applied load diagram for TiN coating wear against AISI M2 high speed steel pins at 0.7 m/s [60]; (b) Steady-state pin temperatures, measured from averaged thermocouple measurements over steady-state temperature regimes, for wear tests at different applied loads [60]; (c) Mean steady-state coefficient of friction, measured from averaged COF readings over steady-state sliding regimes, for wear tests at different applied loads [60].

The transition was accompanied by smoothening of surface asperities in the wear track, a reduction in acoustic emission and coefficient of friction together with overall softening and

rapid wear of the TiN layer. The observed transition from polishing wear and brittle spallation to ductile micro plowing wear mechanisms in the TiN coating cannot alone be attributed to increasing contact stresses in the sliding region between pin and coating.

The transition arises when friction heating effects produce a steady-state pin temperature of approximately 160°C, 3 mm from the interface. This temperature is within the same range of the transition temperature of about 200°C observed for hardness reduction of a TiN-coated austenitic stainless steel subjected to hardness indentation experiments at elevated temperatures. The hot indentation experiments demonstrated that the relaxation in thermal mismatch compressive residual stresses in the TiN is responsible for reductions in the high-temperature hardness [34]. The hardness of the coating was lowered to those of the uncoated substrate at approximately 200°C, indicating that little or no improvement in wear resistance can be expected at this temperature.

According to A. T. Alphas et al. [64], wear rate measurement by mass loss alone underestimates the actual wear damage in that plowing deformation, and the resultant exposure of the substrate is achieved by material displacement and plastic deformation, rather than through material loss by fragmentation or cutting type wear modes. Severe materials transfer and oxidation of wear debris to the coating surface diminish the wear rates measured by mass loss, and this explained the lower wear rate at regime (iii). This kind of transition behaviors of TiN coatings during sliding wear tests have also been observed in [61, 62].

The existing literature reveals that TiN cannot retain its high hardness at elevated temperatures and thus cannot improve the wear resistance of steels at temperatures above 200°C. Thus, another type of hard coatings with improved thermal stability is needed.

#### *2.3.2.3 Characterization of (Ti, Al)N PVD coating*

Then, it comes to the second generation of PVD transition metal nitride coatings. These coating can be divided into two categories:

1) Titanium based (Ti, X)N PVD coatings, where X is usually another metallic element;
2) Chromium based CrN/X-CrN PVD coatings, where X is usually another metallic element doping.

It is expected that (Ti, Al)N coatings have much better performance over single TiN because incorporation of aluminum in TiN coatings improves the oxidation resistance, hardness, strength and thermal stability of the coating. Figure 2.15 shows the change in lattice parameter and surface hardness of $(Ti_{1-x}, Al_x)N$ coatings with increasing aluminum content; the hardness reaches the peak value of 3200 HV at x=0.6 [65].

Substitution of Ti atoms with Al atoms in the B1-NaCl structure of TiN results in (Ti, Al)N phase. As a consequence of this substitution, the TiN lattice parameter gradually decreases with an increasing Al content because the atomic size of Al is smaller than that of Ti. As shown in Figure 2.15, the lattice parameter of $(Ti_{1-x}, Al_x)N$ coatings gradually decreased from 4.23 to almost 4.17 Å with the addition of Al. This suggests that Ti atoms in TiN lattice are substituted by Al atoms of the smaller atomic radius. Both Ti and N atoms in TiN lattice have a coordination number of 6, while the coordination number of Al and N is 4 in AlN [66]. The addition of Al beyond 70% results in a change of crystal structure from NaCl to wurtzite ZnS structure. Coexistence of B1 cubic and B4 hexagonal phases is observed in the composition range of 60–70% Al [66]. The amount of Al at which the structural change occurs is reported to vary from 52 [67] to 70% [65, 66, 68 and 69].

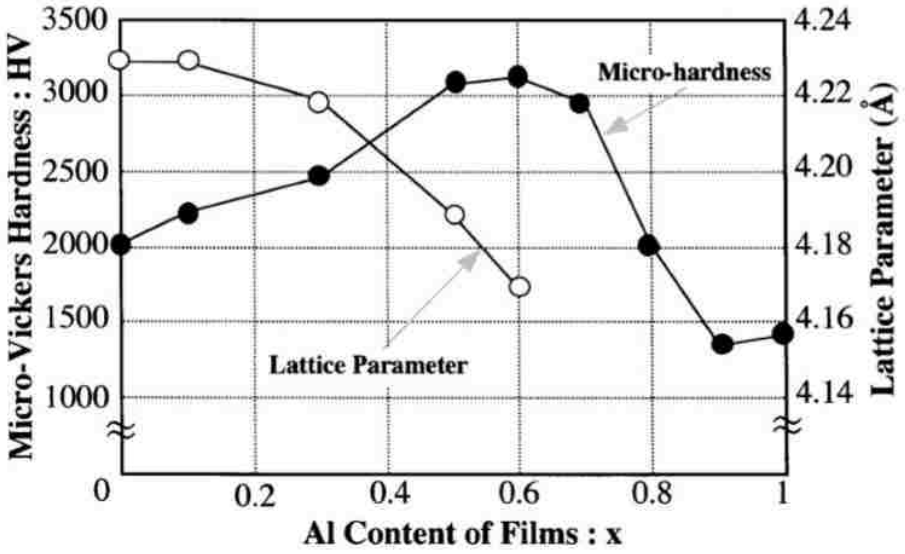


Figure 2.15 Changes in lattice parameter and micro-hardness of $Ti_{1-x}Al_xN$ films with x=0, 0.1, 0.3, 0.5, 0.6, 0.7, 0.8, 0.9, 1.0, respectively. The hardness and lattice parameter of TiN film were ~2000 HV and 4.23 Å, respectively. With the addition of Al into Ti-based targets, the micro-hardness gradually increased up to~3200 HV at x=0.6 and rapidly decreased to~1400 HV at x=0.9 [65].

Kimura et al. [65] studied the maximum solubility of Al in the B1-NaCl structure of $(Ti_{1-x}, Al_x)N$ coating. X-ray diffraction revealed B1-NaCl structure for $(Ti_{1-x}Al_x)N$ where $x \leq 0.6$, and changed to wurtzite structure where $x \geq 0.7$. The change in crystal structure also affected the coating microstructure. SEM revealed a columnar structure up to 60% of Al content. The columnar structure disappeared beyond 60% Al, and grain size became much smaller. A similar observation was made at a higher aluminum region where two-phase structures were present [70]. In the range of $0.5 \leq x \leq 0.66$ AlN phase precipitated along the grain boundaries of cubic (Ti, Al)N.

Microhardness profiles of different titanium based coatings measured at various temperatures are shown in Figure 2.16 [71, 72]. It is interesting to note that TiC and Ti(C, N) possessed higher

hardness at room temperature as compared with either TiN or (Ti, Al)N. They all exhibited a decrease with an increase of temperature, and the reduction of hardness was much more pronounced in the case of TiC. At 1000°C, (Ti, Al)N was considerably harder than TiC and Ti(C, N). The retention of the higher hardness of (Ti, Al)N and Ti(C, N) may partly be attributed to the solid solution effect of Al and C in the TiN lattice.

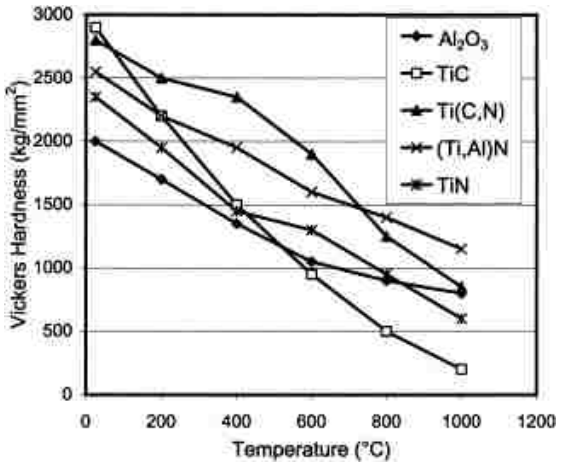


Figure 2.16 Temperature dependence of micro-hardness of Ti(C, N), (Ti, Al)N, TiN, and Al2O3 [71, 72].

High hot hardness significantly improves the abrasive wear resistance of (Ti, Al)N coatings at elevated temperature. The fundamental advantage of (Ti, Al)N is that it exhibits excellent high-temperature stability by forming a dense, highly adhesive, and protective $Al_2O_3$ surface film and prevents diffusion of oxygen into the coating. Its low thermal conductivity allows dissipation of a considerable amount of heat via chip removal [73]. The above two factors allow a higher cutting speed since the thermal loading on the substrate is lower.

Based on this consideration, it has been proposed that CrN should also be able to retain its high hardness at an elevated temperature since it might form a dense, highly adhesive, and

protective $Cr_2O_3$ surface film. This consideration led to the development of another type of high-temperature PVD coating: Chromium based CrN/X-CrN PVD coatings.

### *2.3.2.4 Characterization of CrN PVD coating*

Chromium (III) nitride can be prepared by direct combination of chromium and nitrogen at 800°C: $2Cr + N_2 \rightarrow 2CrN$. It can also synthesize by Physical Vapour Deposition technique such as cathodic arc deposition. Chromium nitride crystallizes in the B1 NaCl structure and exists over a narrow range of composition according to the equilibrium phase diagram as shown in Figure 2.17 [74].

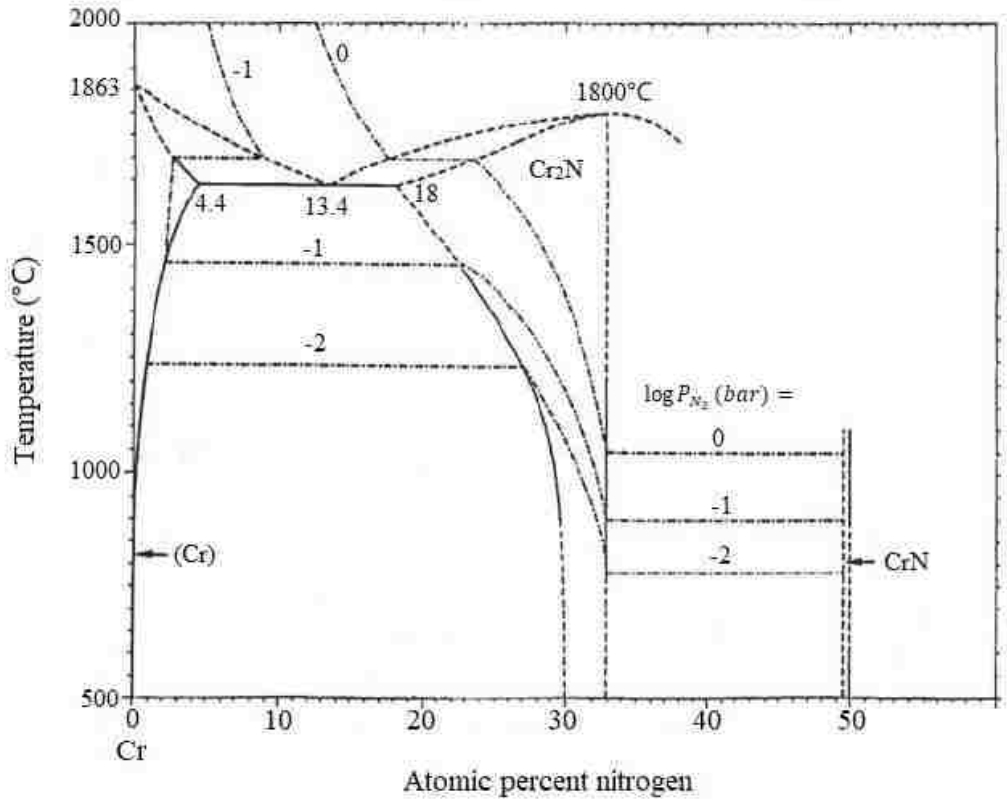


Figure 2.17 Equilibrium phase diagram of Cr-N binary system [74].

A. Ehiasarian et al. [75] utilized high power pulsed magnetron sputtering (HIPIMS) technique to deposit CrN coating on high-speed steel and stainless steel. A residual compressive stress of 3GPa and a hardness value of $HK_{0.025}$=2600 were achieved. T. Polcar et al. [76] studied the properties of CrN coating at temperatures up to 500°C, and claimed that CrN coating could retain its hardness at 500°C, as shown in Figure 2.18.

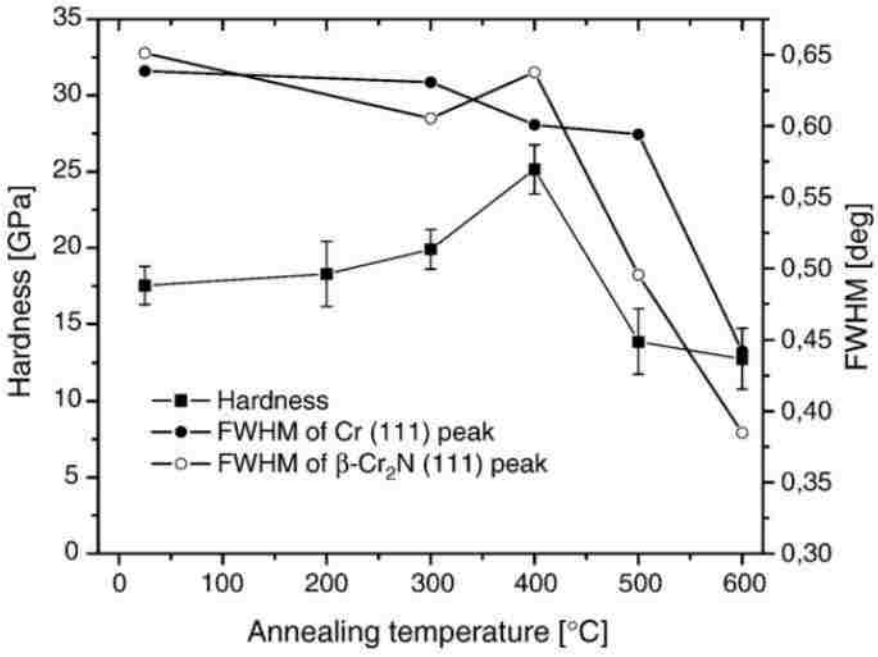


Figure 2.18 Hardness and FWHM of the Cr (111) and β-$Cr_2N$ (111) diffraction peak as a function of annealing temperature [76].

H.C. Barshilia et al. [77] investigated the mechanical properties of (Cr, Al)N coating at a temperature up to 700˚C. They reported the coating had a hardness of 33GPa (tested by nanoindentation) at room temperature and a hardness of 22.5GPa after annealing at 700˚C, showing superior hardness at elevated temperature. Wu et al. [78] studied the influence of Nb addition on the microstructure and hardness of the CrN. It is evident that incorporating the Nb

into the CrN provides a favorable condition for the grain size refinement of the coating, and thus improve the hardness of CrN coating from 15.2 ± 0.6 to 19.1 ± 0.7GPa. Moreover, 0.5 at. % Nb addition would also greatly improve the oxidation resistance of the coating.

CrN-based ternary coatings (CrN films incorporating other elements such as Ti, Al, Si, Mo, W, Nb, etc. [77-82]) have been found exhibiting higher hardness, lower friction coefficients, better thermal stability, and more excellent corrosion resistance than binary coatings. Among these ternary coating systems, W-doped CrN coatings have the great promising friction reducing effect as tungsten could be oxidized during sliding and form the Magnéli phases. The influence of W incorporation on the microstructures and tribological properties has been reported by Chang et al. [83]. The CrWN coating was characterized by high hardness (25GPa), low surface roughness (Ra < 11 nm), and low friction coefficient (varied from 0.15 to 0.3 according to the amount of W addition).

# Chapter 3: Experimental procedures

In this chapter, the trial techniques used for surface modifications (nitriding and duplex treatment) of the hot stamping dies and the study of their wear behaviors are illustrated. As demonstrated in the literature review, the nitriding is used for surface modification of the large die, and the duplex treatment is applied by the "inserts" method for enhancing the forming details and improving the durability at hotspots. In the present study, nitriding was performed on two sets of popular stamping die materials, alloyed steel NAAMS-S0050A and refined pearlitic ductile iron NAAMS-D6510, and the duplex treatment was performed on H13 hot work tooling steel. All the samples were provided by the outside companies. The impact-sliding wear tests were carried on the samples for accelerated wear/failure simulation of the hot stamping dies. The wear tracks were evaluated by the surface profilometer, scanning electron microscope (SEM), energy-dispersive X-ray spectroscopy (EDS), and X-ray photoelectron spectroscopy (XPS) to figure out the wear behaviors and failure mechanisms of the surface modifications.

## 3.1 Sample preparation

### 3.1.1 Nitrided iron/steels

The materials used in the present study were two popular stamping tool materials, a refined pearlitic ductile iron NAAMS-D6510 and an alloyed steel NAAMS-S0050A. They have quite similar mechanical properties but different chemical compositions, as shown in Table 3.1 [84], which may lead to different properties of case hardened layers. For the specimen preparation, two sets of samples were cut into 25.4 mm * 25.4 mm * 5 mm plates and subsequently machined to ensure the same surface finish. The plates were cleaned, degreased, and then nitrided by the plasma nitriding, pulsed plasma diffusion (PPD), and fluidized bed nitriding processes, respectively. The details of nitriding processes are summarized in Table 3.2.

Table 3.1 Chemical composition and mechanical properties of ductile iron and cast steel [84].

| Materials | | D6510 | S0050A |
|---|---|---|---|
| Element (wt.%) | C | 3.41 | 0.45 |
| | Si | 2.22 | 0.36 |
| | Mn | 0.41 | 1.05 |
| | Mo | 0.42 | 0.41 |
| | Cu | 0.56 | – |
| | Ni | 1.12 | – |
| | Cr | 0.10 | 0.90 |
| | S | 0.02 | 0.03 |
| | P | 0.04 | 0.03 |
| | V | – | 0.12 |
| | Mg | 0.05 | – |
| | Fe | Balance | Balance |
| Yield strength (MPa) | | 570 | 585 |
| Tensile strength (MPa) | | 350 | 310 |

Table 3.2 Some parameters of the nitriding processes*

| Nitriding techniques | Processing parameters | | |
|---|---|---|---|
| Plasma nitriding 1 (A**) | Temperature (˚C) | Time (hrs.) | Total pressure (mabr) |
| | 570 | 4 | 2.9 |
| | Partial pressure of nitrogen (mbar) | | Partial pressure of methane (mbar) |
| | 1.45 | | 0.058 |
| Plasma nitriding 2 (B**) | Temperature (˚C) | | Time (hrs.) |
| | 540 | | 17 |
| | Gas mixture | | |
| | 99.4% $H_2$, 0.6% $N_2$ | | |
| Pulsed plasma diffusion (C**) | Temperature (˚C) | | Time (hrs.) |
| | 540 | | 17 |
| | Gas mixture | | Pulse (sec.) |
| | 99.4% $H_2$, 0.6% $N_2$ | | 0.48/0.02 |
| Fluidized bed nitriding (D**) | Temperature (˚C) | | Time (hrs.) |
| | 575 | | 12 |
| | Gas mixture | | Fluidized bed materials |
| | 60% $NH_3$, 40% $N_2$ | | $Al_2O_3$ particles |

* As required by the companies, details of the key parameters will not be included in this table;
** Represent the companies which provided the samples.

### 3.1.2 Duplex treatment on H13 hot work steel

Duplex treatment on H13 hot work steel is usually used as inserts to enhance the forming details and extend the lifetime of hot stamping dies. In the present study, H13 steel (Table 3.3) coupons with a size of 50mm×50mm×6mm were prepared, polished to Ra=0.02μm, and then ultrasonically cleaned in ethanol.

Table 3.3 Mechanical properties and chemical composition of H13 hot work steel [85].

| | | |
|---|---|---|
| Hardness (HRC) | 52-54 | |
| Yield strength (MPa) | 1650 | |
| Tensile strength (MPa) | 1990 | |
| Elements (wt. %) | C | 0.32-0.40 |
| | Mn | 0.20-0.60 |
| | Cr | 5.13-5.25 |
| | Mo | 1.33-1.40 |
| | Si | 1 |
| | V | 1 |
| | Fe | Balanced |

After hardened and tempered, the coupons were nitrided using plasma nitriding technique. Nitriding cases with a surface hardness of 1200 HV0.2 and a thickness of about 120μm were achieved. W-doped CrN coatings were then deposited on the nitrided substrates using a cathodic arc evaporation technology at 350°C. To fairly evaluate the wear properties of these W-doped

CrN coatings; all the processes adopted the commercially used parameters. As required by the company, details of the key parameters will not be presented here

### 3.2 Surface roughness test

The surface roughness Ra (μm) of the modified surface was measured by the surface profilometer (Mitutoyo SJ-201P, Figure 3.1) with a data-summarized system.

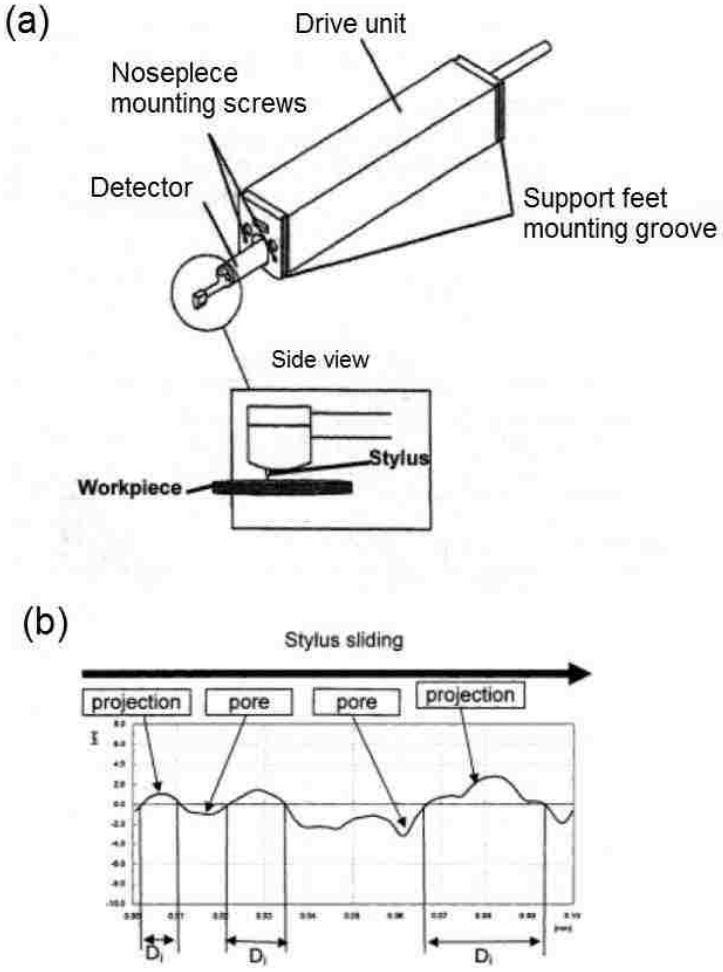


Figure 3.1 Mitutoyo SJ-201P surface profilometer: (a) the detector, and (b) a characteristic surface profile plot [86].

### 3.3 Surface hardness, hardness profiles and elastic modulus measurement

Metallographic sections were examined using an optical microscope (Figure 3.2.a) and a scanning electron microscope equipped with an EDS detector (FEI Quanta 200 FEG, Figure 3.2.b). The surface hardness of all modified surfaces was measured by a microhardness tester (Figure 3.3) with indentation load 0.0981 N. Meanwhile, for the nitrided iron/steels, the hardness profiles were also determined with indentation load 0.245 N.

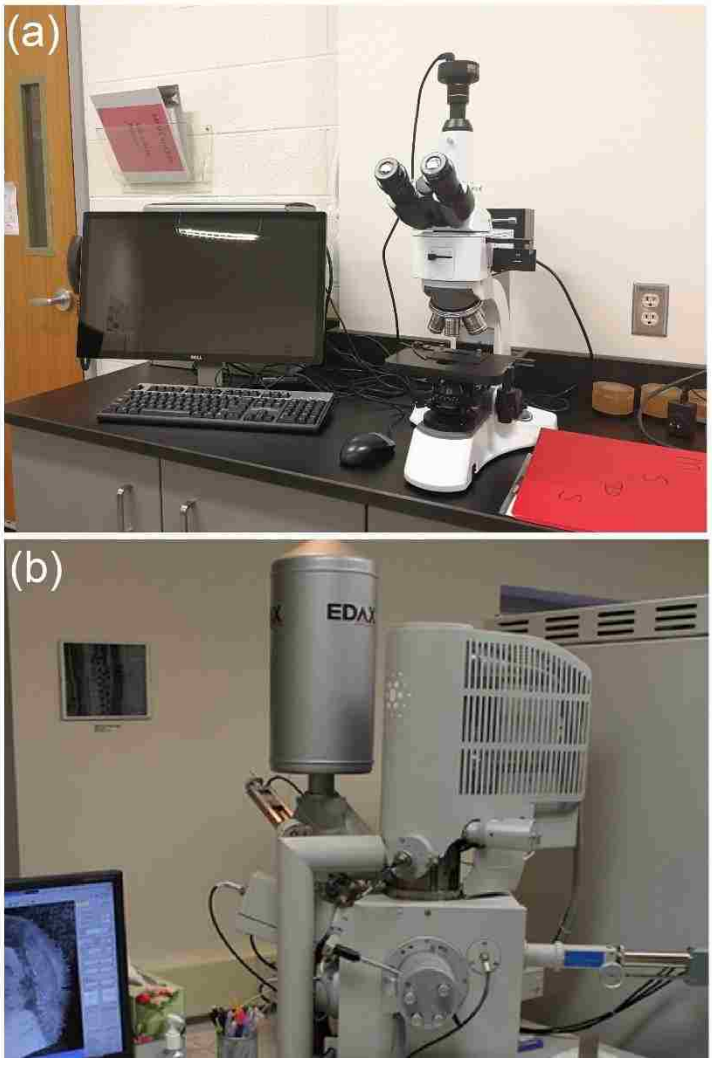


Figure 3.2 (a) Optical microscope, and (b) Scanning Electron Microscope (FEI Quanta 200 FEG) used in the present study.


Figure 3.3 Buehler MicroMet II micro-hardness tester.

The elastic modulus was measured by Hysitron nanoindentation machine (Figure 3.4) with a load of 2500 μN.

Figure 3.4 Hysitron nanoindentation machine.

### 3.4 Inclined impact-sliding wear test

#### 3.4.1 Room temperature wear test for nitrided iron/steels

As mentioned in the literature review, the nitrided surface was not supposed to work under elevated temperature. Thus, in the present study, the nitrided iron/steels were evaluated by our first-generation room temperature inclined impact-sliding wear tester (Figure 3.5). To start an impact-sliding test, the flat specimen is secured on the sample holder. The sample holder functions as a rocker that can rotate around a fixed roller bearing due to the pressing of the steel

ball when the piston moves up and down. Driven by the piston, the ball pushes downward against the flat specimen, causing sliding between the ball and the flat specimen in the first half of each test cycle. After a short pause at the end of the sliding scar, the ball slides reversely on the surface of the flat specimen and is then disengaged from the surface in the second half of the test cycle. For all the tests, the counterparts were SAE 52100 steel balls (60-62 HRC).

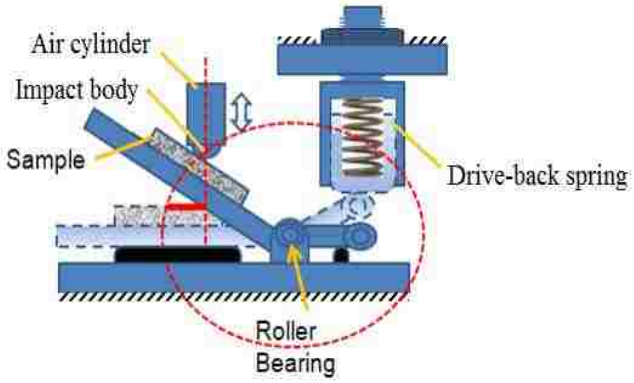


Figure 3.5 Setup illustration of the room temperature cyclic inclined impact-sliding wear tester.

An OMEGA LCKD-500 load cell was placed on the sample holder to calibrate the normal load curve on the sample surface during the impact-sliding movement. The desired normal load curve could be obtained by adjusting the pre-strain of the spring and the stroke distance. The calibrated load curve is illustrated in Figure 3.6 (a).

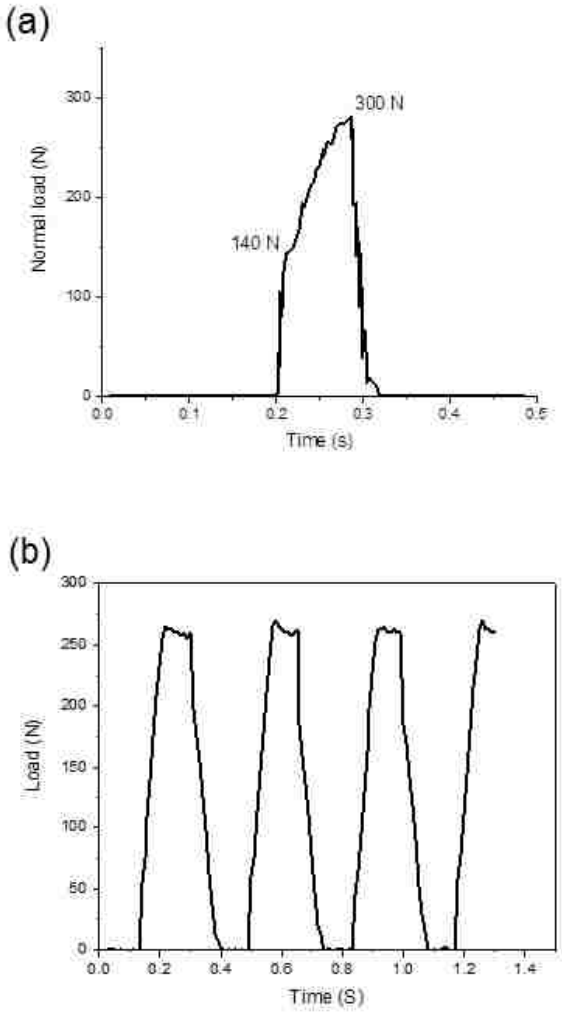


Figure 3.6 Calibrated load curves of inclined impact-sliding wear tests for (a) nitrided iron/steels, and (b) duplex treatment on H13 steels.

### 3.4.2 Wear test for duplex treatment at room and elevated temperatures

As discussed in the literature review, the utilization of duplex treatment on the hot stamping dies mainly aims to improve the forming details and combat with the "hot spots" caused by inhomogeneous temperature distribution. To evaluate the performance of duplex treatment during hot stamping process, a second-generation high temperature inclined impact-sliding wear tester (Figure 3.7) was developed to simulate its working condition.

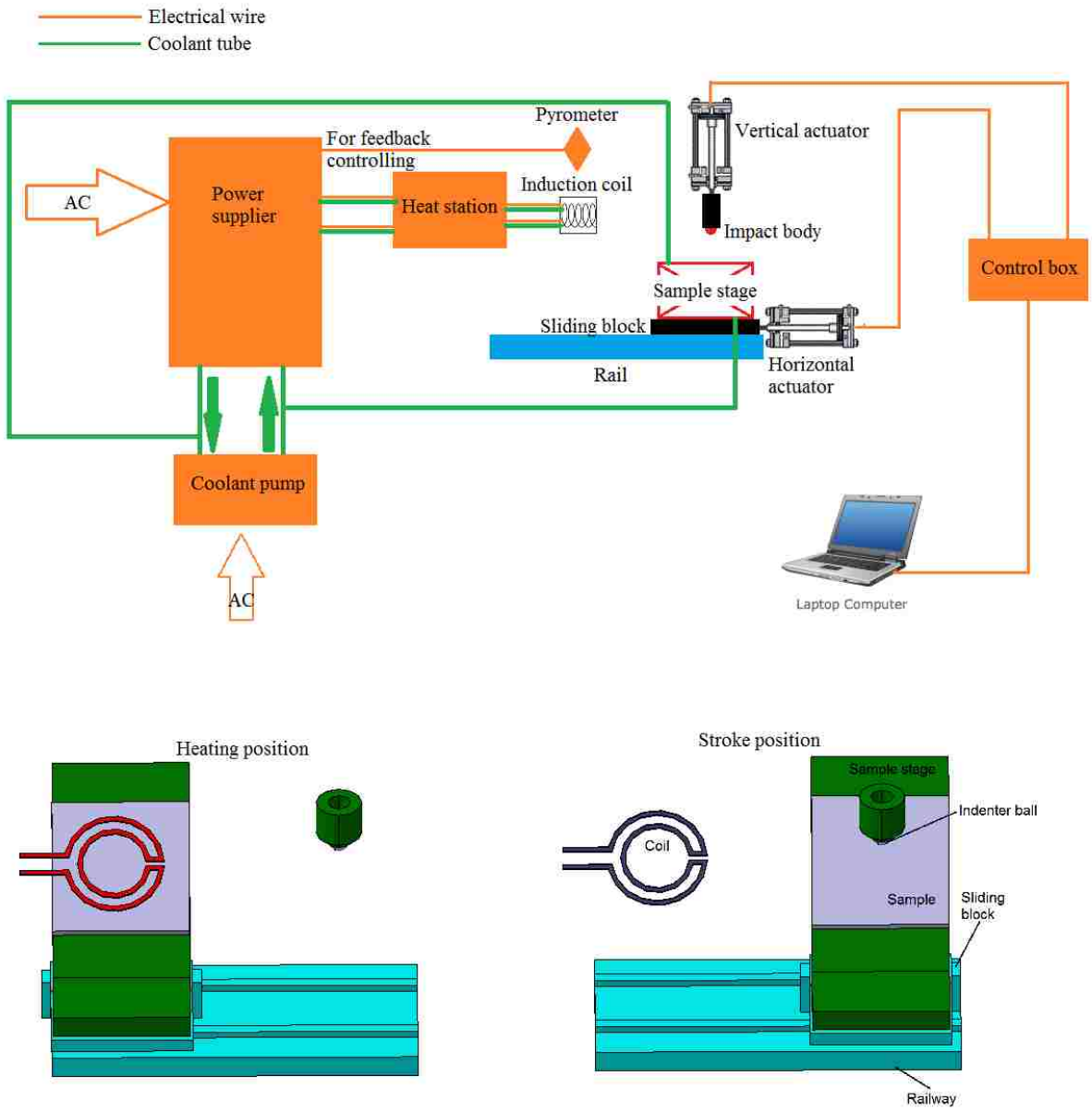


Figure 3.7 Setup drawing of the high temperature inclined impact-sliding wear tester.

A high temperature inclined impact-sliding wear tester was developed for the present research. The tester consists of three main parts: (i) inclined impact-sliding system; (ii) induction heating system; and (iii) cooling system. The inclined impact-sliding system works similarly with the first-generation machine, except using an actuator to replace the air cylinder. During the

test, a hardball was mounted on the shaft of the vertical actuator which pushed against the sample surface. The sample was set in an inclined rotary sample holder that can return its original position by a spring. The calibrated load curve is illustrated in Figure 3.6 (b).

The samples were scheduled to be tested 2000 cycles without lubricant at room temperature and 400°C, assuming the local temperature of the "hotspots" on the die surface could reach up to 400°C during the hot stamping of the AHSS. The temperature was measured and controlled via a pyrometer and feedback controller built in the induction heating system (8 KW). For each cycle tested at elevated temperature, the sample was firstly heated up to 400°C and held for 2s at the heating position. Then the sample was moved along the railway to the stroke position for the impact-sliding wear test, after which the sample was moved back to the heating position for the next cycle. The total time for one cycle of test at 400°C was about 2.7s. The temperature of the sample holder during the test was maintained to be lower than 80°C by the cooling system, which intended to have a temperature gradient simulating the press hardening operation in hot stamping. The test frequency at room temperature was set as the same as the frequency for the 400°C case to exclude the influence of the testing frequency. For all the tests in this work, M50 hardened steel ball (62HRC, hot work steel) was used as the counterpart material. This steel was chosen because it would not soften at 400°C, which is beneficial for maintaining the contact stresses to be the same at room and elevated temperatures.

### 3.5 Characterization of the worn surfaces

After the wear tests, the samples were removed from the facilities and carefully cleaned by acetone, deionized water and ethanol to remove the loose wear debris. Then, surface profilometer was used to measure the wear tracks. Scanning electron microscope was utilized to observe the topography of the worn surfaces. EDS analysis was carried out to figure out the composition of

the wear products. All the information was summarized and analyzed to evaluate the wear and failure mechanisms of the surface modifications.

X-ray photoelectron spectroscopy (XPS, Kratos AXIS NOVA, Figure 3.8) analysis was also carried on the duplex treatment samples to figure out the possible evolution of the surface properties at elevated temperature. The XPS analyses were carried out with a monochromatic Al K(alpha) source (15mA, 14kV), which can probe the surface of the sample to a depth of 5-7 nanometers. The instrument work function was calibrated to give a binding energy (BE) of 83.96 eV for the Au 4f7/2 line for metallic gold, and the spectrometer dispersion was adjusted to give a BE of 932.62 eV for the Cu 2p3/2 line of metallic copper. Specimens were electrically isolated during the analyses, and the Kratos charge neutralizer system was used on all specimens.

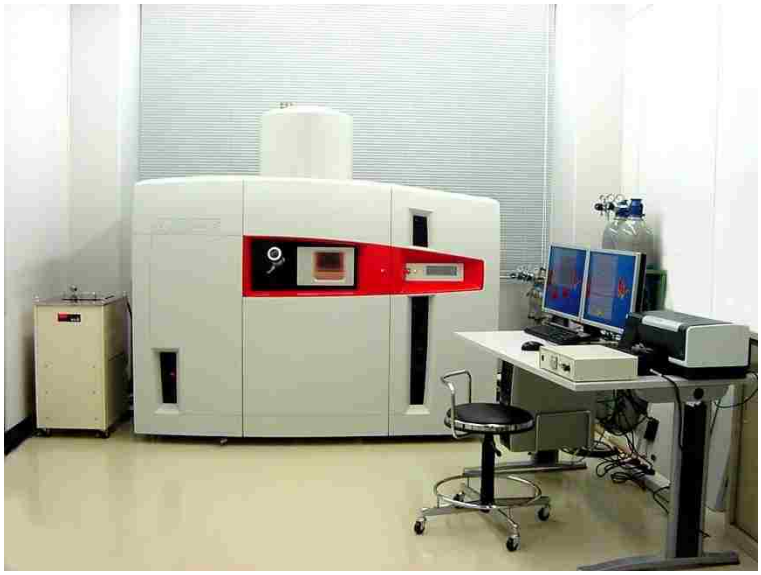

Figure 3.8 Kratos AXIS NOVA X-ray photoelectron spectroscopy.

Away from the wear track, survey scan analyses were carried out with an analysis area of 300 x 700 microns and a pass energy of 160 eV, and then high-resolution analyses were carried out with a pass energy of 20 eV. Inside the wear track, analysis area with a size of 400 x 400

microns was used. Spectra have been recorded and corrected to the main line of the carbon 1s spectrum (adventitious carbon) set to 284.8 eV. Spectra were analyzed using CasaXPS software (version 2.3.14). The fitted Cr 2p peak spectra and W 4f peak spectra were measured and fitted.

# Chapter 4: Inclined impact-sliding wear tests for nitrided ductile iron NAAMS-D6510 and cast steel NAAMS-S0050A

In this chapter, the results of the wear tests for the nitrided ductile irons and steels are presented and discussed (4.1). One typical case of pulse plasma diffusion nitrided iron/steel will be investigated in more details to figure out the wear and failure mechanisms (4.2). The cross-sectional hardness and nitrogen concentration profiles of the treated iron and steel were obtained. Pin-on-disk and inclined sliding wear tests were used to evaluate their tribological properties under different loading conditions. Surface profilometer and scanning electron microscopy were employed to measure and observe the wear tracks. It was found that the treated ductile iron sample behaved similarly in the two test methods while the treated cast steel sample showed different wear mechanisms. This phenomenon was attributed to the different characteristics of the nitrogen diffusion zones; a larger gradient of nitrogen concentration in the case hardened layer of the steel sample could lead to a relatively high risk of surface fatigue cracking under the highly stressed inclined sliding test condition.

## 4.1 Inclined impact-sliding behavior of the nitrided irons and steels

The nitrided samples prepared in Chapter 3 were tested by inclined impact-sliding wear test under the calibrated load curve (Figure 3.6.a) for 500 and 1000 cycles. Then, according to the behaviors of the samples, tests with more or less cycles were carried out. Finally, the nitrided iron samples were tested for 500, 1000, 1500, and 2500 cycles; and the nitrided steel samples were tested for 100, 250, 500, and 1000 cycles. For simplicity, the samples were referred as S1A, S1B, S1C, S1D, S2A, S2B, S2C, and S2D. Here, “S” represents sample, “1” and “2” represent

ductile and cast steel, respectively. “A”, “B”, “C” and “D” represent plasma nitriding 1, plasma nitriding 2, fluidized bed nitriding, and pulsed plasma diffusion nitriding, respectively.

The wear volume losses were measured by the surface profilometer, as shown in Figure 4.1. The profiles of the wear track were measured and the section areas were calculated by the software, then the volume loss could be calculated by Equation 4.1.

$$V_w = 0.001 * 0.254 * \sum_0^N S_i \ (mm\text{^}3) \tag{4.1}$$

where $V_w$ is the wear volume loss, $S_i$ is the section area of the $i$-th measurements along the wear track, as demonstrated in Figure 4.1.

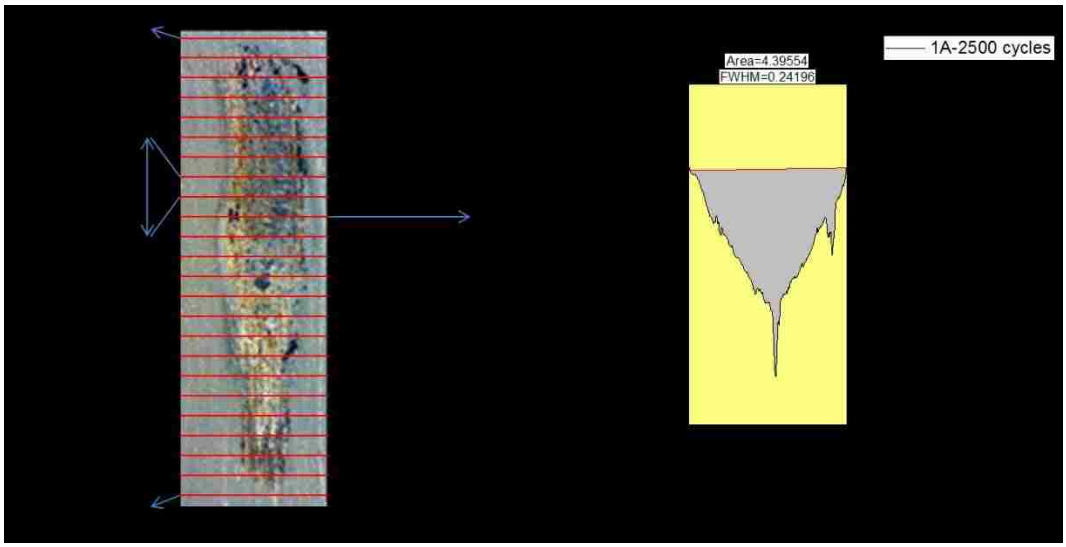


Figure 4.1 Setup illustration of measuring wear volume loss.

The results were summarized in Figure 4.2, from which we could find that for all nitriding techniques, the nitrided irons outperformed the nitrided steels. For the nitrided steel samples, the wear curves could be divided into three sections:

1) Section 1: 100-250 cycles, with a small slope ;
2) Section 2: 250-500 cycles, with a large slope;
3) Section 3: 500-1000 cycles, with a small slope.

For the nitrided iron samples, the slopes of the curves seemed to be constant.

The wear rates defined as:

$$W_R = V_w / E_s \tag{4.2}$$

where $W_R$ is the wear rate, $V_w$ is the wear volume loss, and $E_s$ is the total sliding energy.

The wear rates were calculated for the nitrided irons and all three sections of the nitrided steels. The results are summarized in Figure 4.3. From which we could find that during section 2 (except B, plasma nitriding 2), the wear rates were one order higher than the wear rates of the nitrided irons.

Among all the samples, the pulsed plasma diffusion nitrided ductile iron (S1D) had the highest wear resistance, while the cast steel nitrided by the same technique had the worst wear resistance. Therefore, these two samples are chosen for the detailed case study.

Figure 4.4 shows the optical images of the wear tracks, from which we can see that the wear tracks of the nitrided steel samples were wider and deeper than those of the nitrided iron samples.

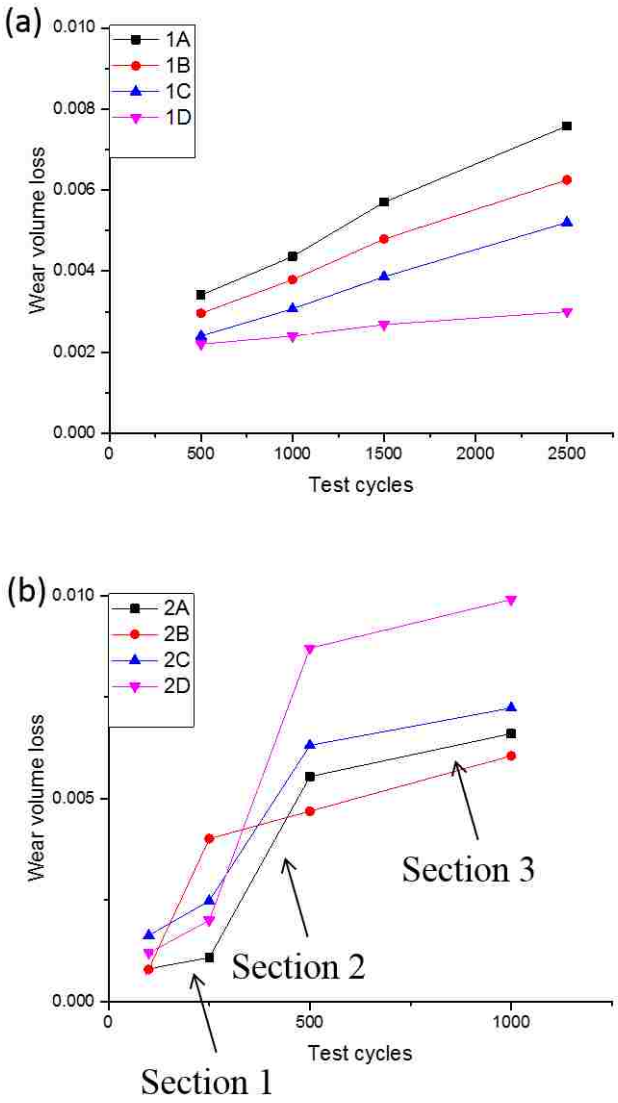


Figure 4.2 Wear volume loss vs. test cycles curves for nitrided die materials (a) D6510, and (b) S0050A.

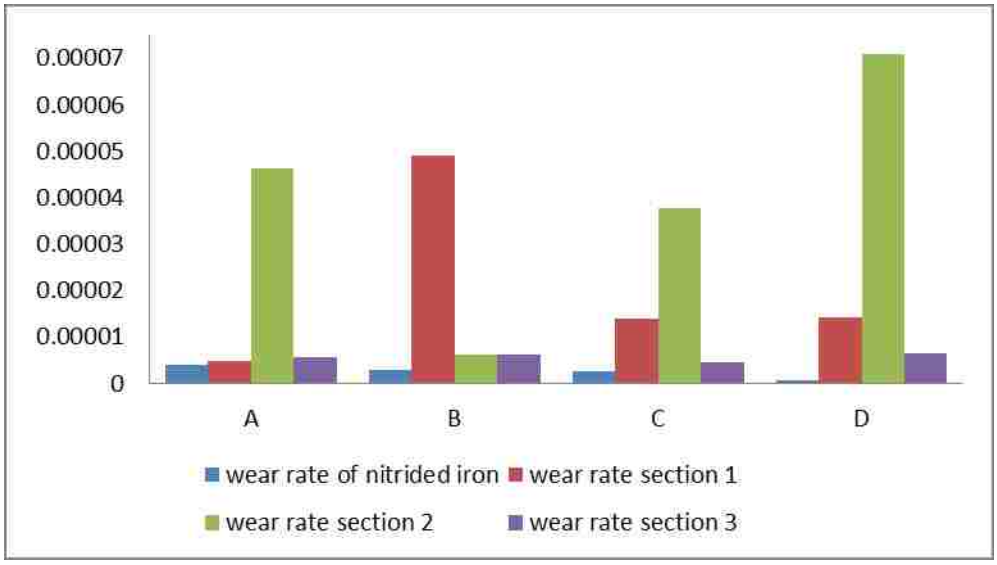


Figure 4.3 Wear rate plots for the nitrided irons and all three sections of the nitrided steels.

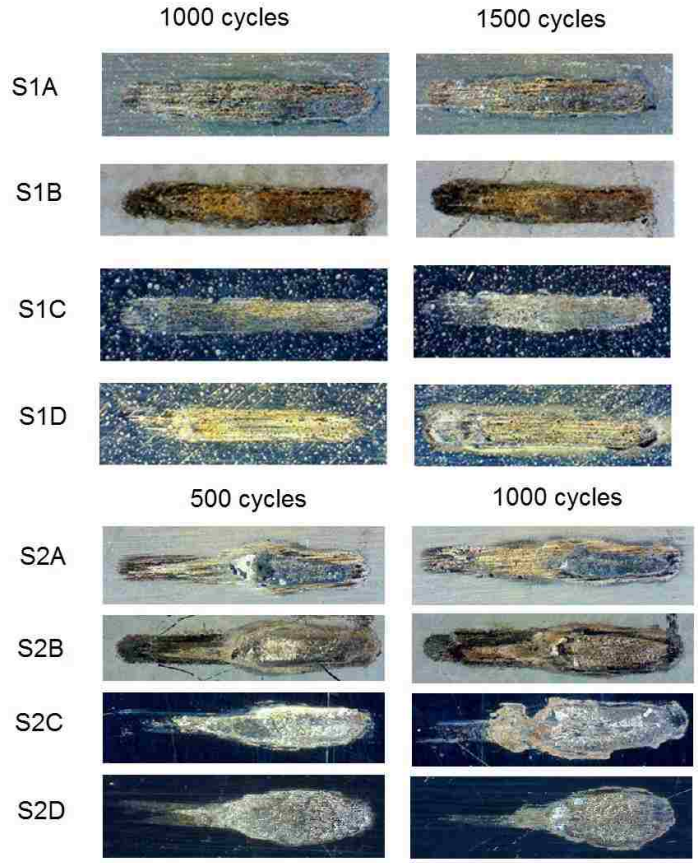


Figure 4.4 Optical images of the wear tracks for the nitrided irons and steels.

## 4.2 A case study of pulse plasma diffusion nitrided iron/steel

For the simplicity, the nitrided iron is called TI while the nitrided steel is called TS.

### 4.2.1 Characterization of the case hardened layers

The Vickers hardness measured on the surface of the samples was reported in Table 4.1. These values are the average of five measurements. TI and TS samples had almost the same surface hardness. Figure 4.5 (a) shows the hardness profiles below the surfaces. It is intriguing to point out that at a depth of around 15 μm (boundary of the compound layer and diffusion zone), the slopes of hardness profiles started to be significantly different. The slope of the hardness profile of the TI sample is obviously smaller than that of the TS sample. Moreover, the nitriding depth of the TI sample (about 170μm) was higher than that of the TS sample (about 120μm). Which means the hardness degrading of the TS sample was much quicker than that of the TI sample.

Figure 4.5 (b) shows the nanoindentation tests for the TI and TS samples, from which we could find that the compound layer for both samples had similar hardness and elastic modulus. However, the characteristics of the diffusion zones were significantly different. The diffusion zone of the TI sample had a hardness and an elastic modulus more close to those of the compound layer, as summarized in Table 4.1. That is to say the modulus degrading of the TS was also much quicker than that of the TI sample.

Figure 4.6 shows the optical microscopy images of the section area of TI and TS samples after etching with 2% Nital solution. The optical examination of the metallographic sections revealed that: both samples had a thin compound layer on the top of a diffusion zone; the microstructures of diffusion zones of TI and TS samples were obviously different, which might

explain the difference of hardness profiles. The thickness of compound layers and the nitriding depth were also double-checked by the optical analysis; the results were summarized in Table 4.1.

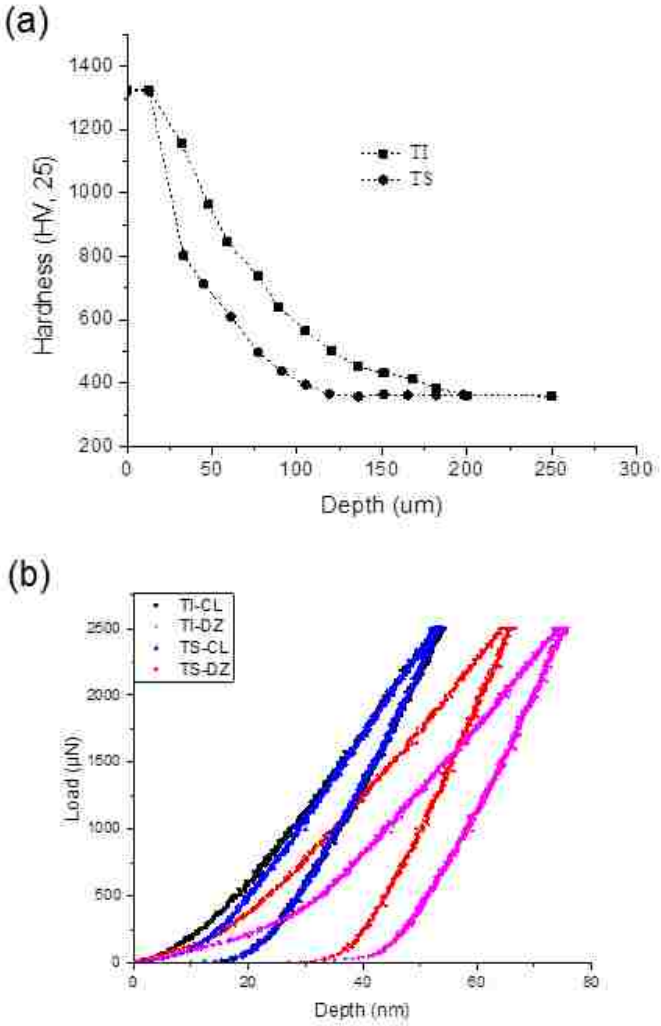


Figure 4.5 (a) Cross-sectional hardness profiles of the TI and TS samples; (b) Nanoindentation load-displacement curves for the compound layer of the TI sample (TI-CL) and TS sample (TS-CL), as well as for the diffusion zone of the TI sample (TI-DZ) and TS sample (TS-DZ).

Detailed analysis on the origination of the difference of the case-hardened layers has exceeded the scope of this study. However, it is evident that the different nitrogen concentration profiles played an important role in the difference of the case-hardened layers. More detailed research needs to be carried on this area.

Table 4.1 Characteristics of nitrided layers.

| Sample No. | TI | TS |
|---|---|---|
| Surface hardness (HV) | 1325 | 1321 |
| Compound layer thickness (μm) | 10-12 | 13-15 |
| Nitriding depth (μm) | 170±15 | 120±11 |
| Elastic modulus of the compound layer (GPa) | 298.8 | 295.8 |
| Elastic modulus at the depth of 30 μm (GPa) | 265.8 | 234.3 |

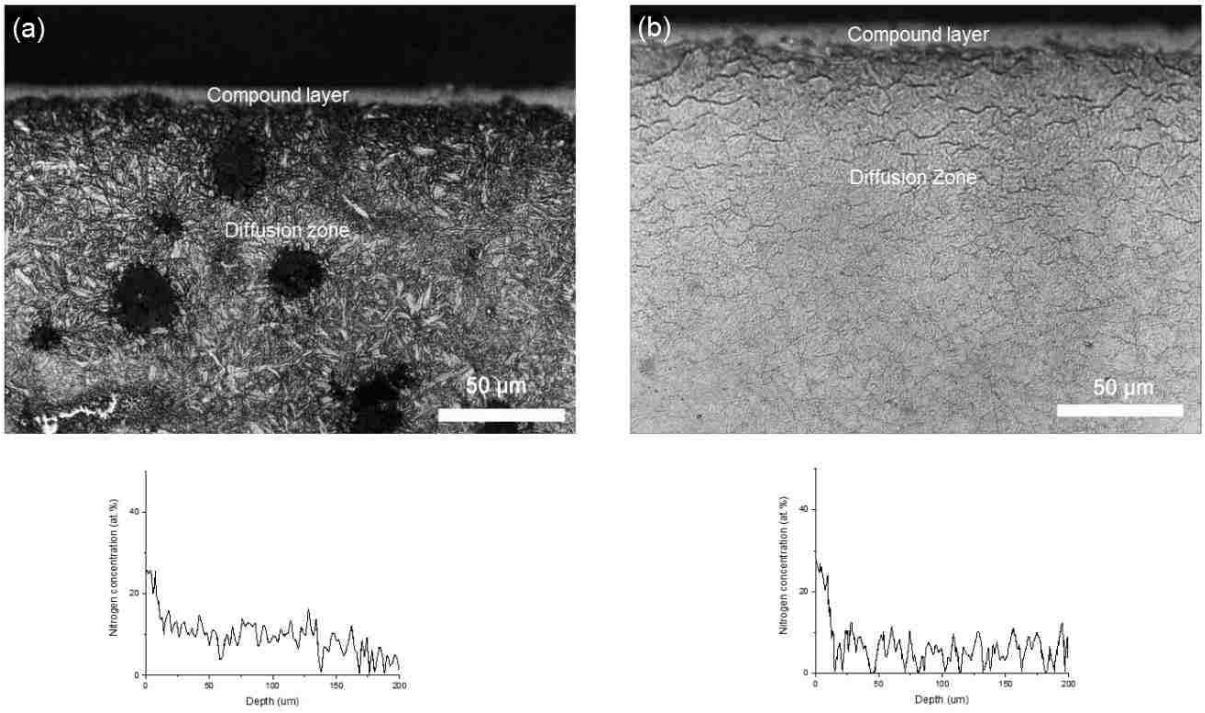


Figure 4.6 Optical images and nitrogen concentration profiles of TI and TS samples, showing the existence of the compound layer as well as the diffusion zone. These two samples had very different nitrogen concentration profiles as well as microstructures in the diffusion zones.

### 4.2.2 Tribological tests

#### *4.2.2.1 Pin-on-disk tribological tests*

Figure 4.7 shows the coefficients of friction of the TI and TS samples under the unlubricated POD sliding conditions against hardened SAE 52100 steel balls. The TI sample presented a lower friction coefficient (0.4 ± 0.1) than the TS sample (0.7 ± 0.02); the COF curve of the TI sample fluctuated more compared to the TS sample. This phenomenon could be attributed to the periodic adhesion and detachment of the graphite (as shown in Figure 4.9.a and 4.9.c) on the contact surfaces of the TI sample and steel ball.

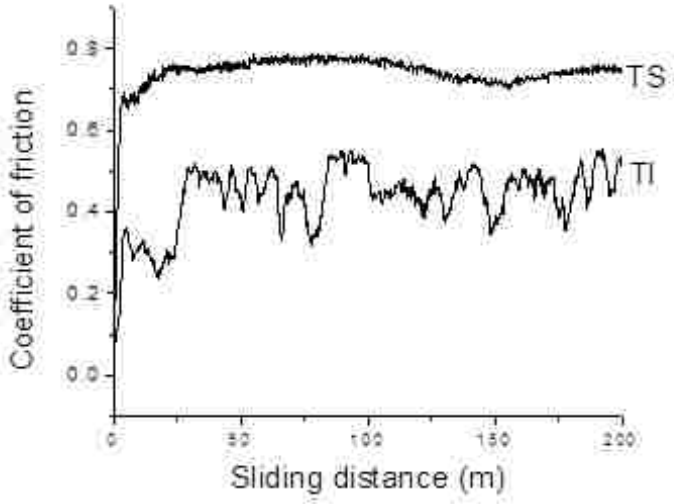


Figure 4.7 Coefficients of friction for pulsed plasma diffusion nitrided samples.

Figure 4.8 shows the volume losses of the TI and TS samples during unlubricated POD sliding wear tests. The TI sample had a lower volume loss than the TS sample. This could be attributed to the lower coefficient of friction, which leads to a lower sliding energy applied on the TI sample surface during the wear test.

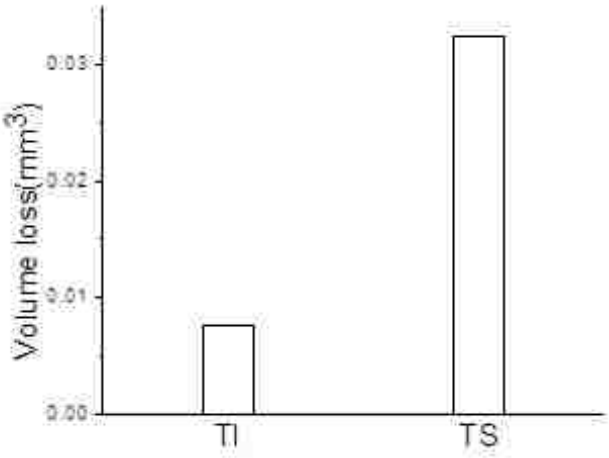


Figure 4.8 Wear volume losses of pulsed plasma diffusion nitrided samples during pin-on-disk wear tests.

SEM observations, illustrated in Figure 4.9, indicate that the wear of the nitrided cast iron and steel mainly consisted of mild abrasive wear, polishing of the sample surfaces, and some materials transferred from the steel balls. The high surface hardness and the high compressive residual stress in the compound layer resulted in improved wear resistance. For the TI sample, slightly abrasive wear and polishing of the nitrided surface were predominant. Materials transfer and wear debris pile-up mainly occurred at the sites where the graphite was originally located. For the TS sample, polishing of the nitrided surface and a small amount of materials transfer exhibited on the worn surface. No surface fatigue cracking was observed on any of the treated samples. Similar wear track morphologies and wear mechanisms have been reported by other researchers.

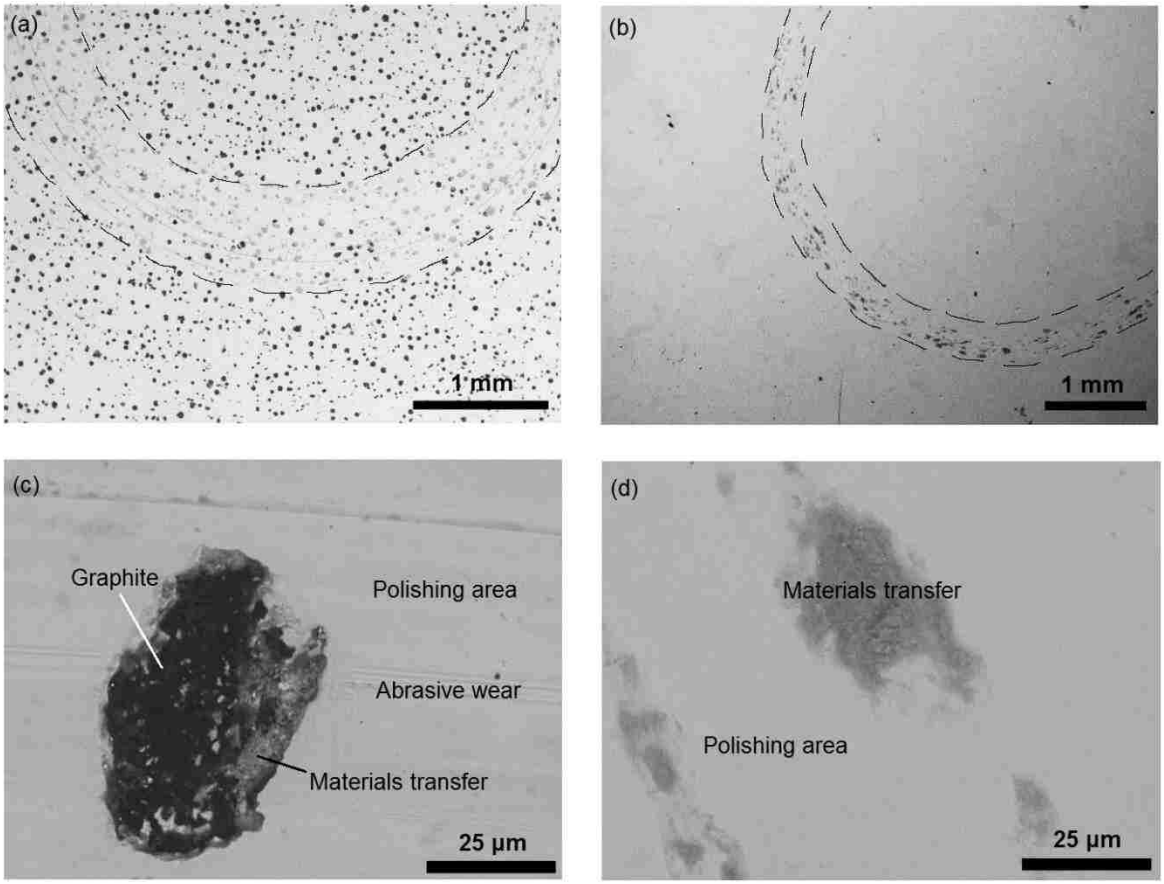


Figure 4.9 SEM morphologies of wear tracks after POD sliding test: (a) and (c) TI sample; (b) and (d) TS sample. The dashed line shows the boundary of the worn surface.

#### *4.2.2.2 Inclined impact-sliding tribological tests*

The nitrided samples were then tested by the inclined impact-sliding wear tester under extremely high contact stress. The wear volume losses at different test cycles were plotted in Figure 4.10. Compared with the TS sample, the TI sample had a much lower wear volume loss even after 2500 test cycles, indicating that the nitrided ductile iron outperformed the nitrided cast steel under high-stressed inclined sliding condition. To figure out the wear mechanisms of the TI and TS samples under high-stressed inclined sliding condition, SEM observation was carried out.

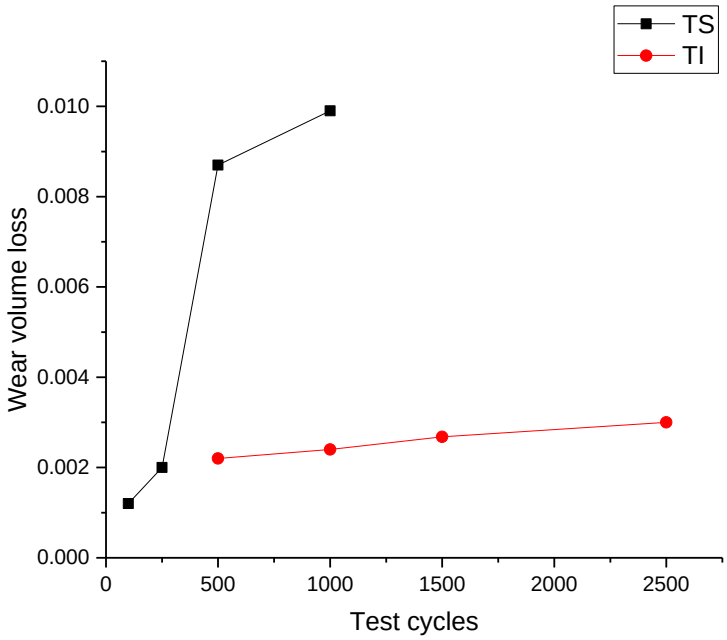


Figure 4.10 Curves of wear volume losses versus number of test cycles of TI and TS samples.

The worn surfaces of the TS sample after 500 test cycles and the TI sample after 2500 test cycles were examined by SEM observation, shown in Figures 4.11 and 4.12.

Figure 4.11 shows the detailed SEM morphology of the worn surface of the TS sample after 500 test cycles; B, C, D, and E represent the head area, middle area, tail area, and the edge of the wear track, respectively. The head area of the wear track on the TS sample appears to have numerous fatigue cracks and small areas of chipping, as shown in Figure 4.11 (b). The middle area of the wear track contained vast areas of chipping and a few residual fatigue cracks after chipping, as shown in Figure 4.11 (c). The tail area of the wear track was mainly characterized by large areas of materials transfer and wear debris pile-up, as shown in Figure 4.11 (d). Figure 4.11 (e) demonstrates the arrangement of the EDS point analysis of area E- the edge of the middle area of the wear track, and the results of EDS analysis are shown in Table 4.2. During the analysis, only Fe, O, and N were measured. This was to enhance the contrast of the EDS results.

Spot 1 had a nitrogen atomic percentage as high as 34% without the appearance of oxygen, indicating the existence of a compound layer. Spots 2 and 4 had lower nitrogen atomic percentages of 9.8 and 7.5%, which was consistent with the nitrogen concentration in the diffusion zone, indicating the removal of the compound layer and exposure of the diffusion zone. Spot 3 had an oxygen atomic percentage of 33% without the appearance of nitrogen, indicating the oxidation and pile-up of wear debris on the surface where the diffusion zone was exposed after the removal of the compound layer.

Table 4.2 Results of EDS analysis in the middle area of the worn surface of TS samples after 500 test cycles

| Element | Atomic percentage (%) | | | |
|---|---|---|---|---|
| | Spot 1 | Spot 2 | Spot 3 | Spot 4 |
| Nitrogen | 34 | 9.8 | NA | 7.5 |
| Oxygen | NA | NA | 33 | NA |
| Iron | 76 | 90.2 | 67 | 92.5 |

Note: Because of the nature of the problem, only nitrogen, oxygen, and iron were chosen during the EDS analysis

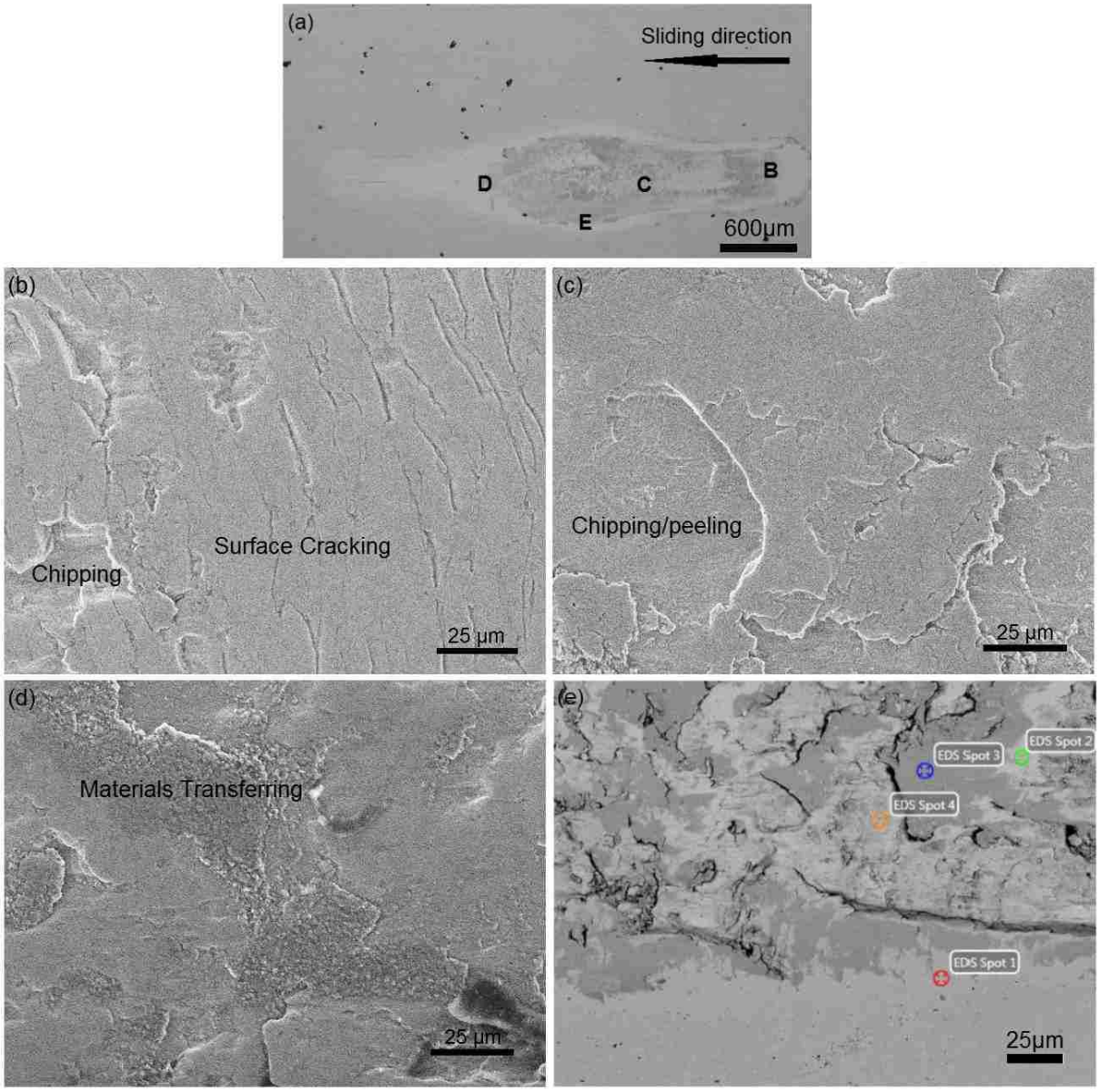


Figure 4.11 Worn surface of the TS sample after 500 test cycles: (a) overview of the wear track at magnification ×30; (b) head area; (c) middle area; (d) tail area; (e) locations of EDS point analysis at the edge of the middle area, where spot 1 was the reference point.

Figure 4.12 shows the detailed SEM morphology of the worn surface of the TI sample after 2500 test cycles. B, C, and D represent the head area, middle area, and tail area of the wear track, respectively. All these areas showed surface fatigue cracks and materials transferred from the

steel ball; most of the materials transferring occurred at the sites where graphite was originally located. No chipping or peeling was found. The wear mechanism mainly consisted of slightly abrasive wear, which was similar to the wear behavior during the POD sliding tests.

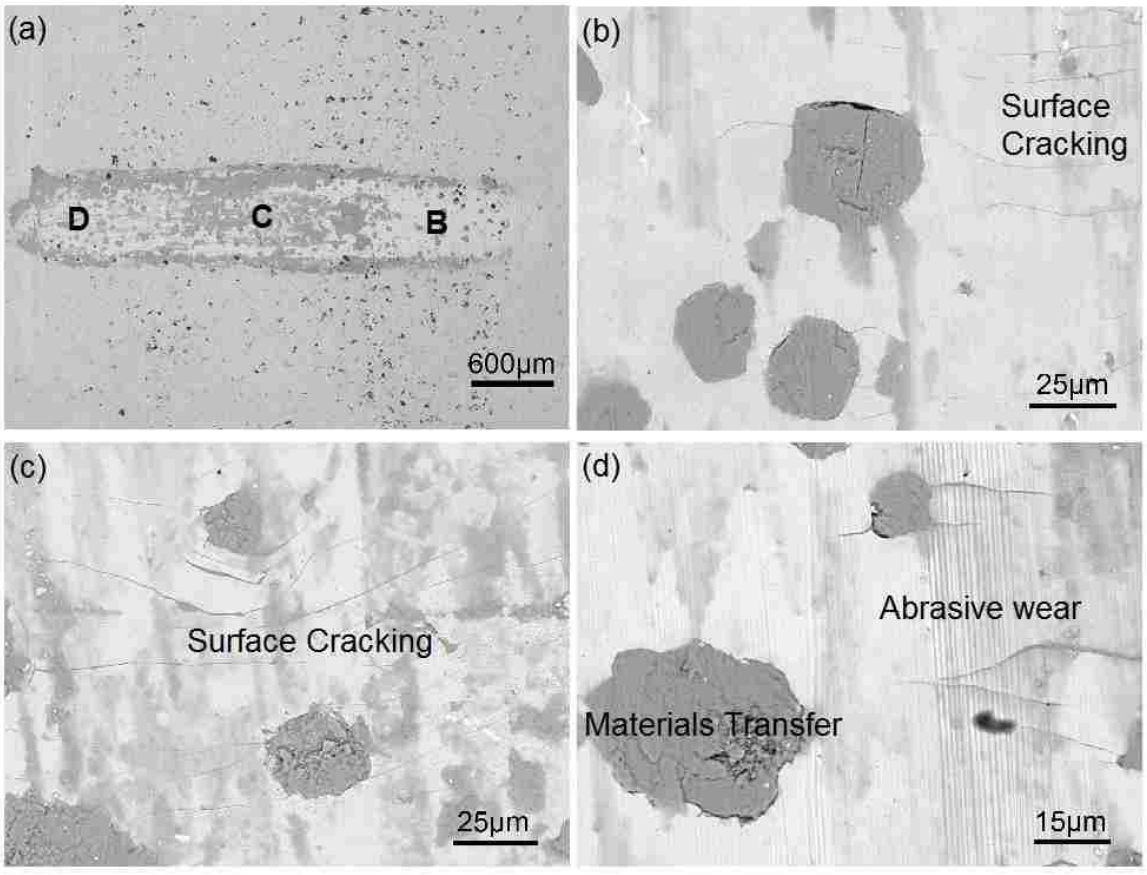


Figure 4.12 SEM morphology of the worn surface of the TI sample after 2500 test cycles: (a) overview of the wear track at magnification ×30; (b) head area; (c) middle area; (d) tail area.

For the TS sample, at the first stage (less than 500 cycles of test) the wear mainly consisted of chipping and peeling of the compound layer, thus the wear rate was relatively high. Later on, during the second stage (more than 500 cycles of test) the compound layer has been peeled off and the wear mainly consisted of abrasive/adhesive wear on the diffusion zone, the wear rate also decreased. However, the hardness of the diffusion zone of the TS sample was pretty low,

therefore, the wear rate was still pretty high. On the contrary, the compound layer of the TI sample was still attached to the diffusion zone, no chipping or peeling was observed even after 2500 cycles of test. The wear of the TI sample was mainly characterized by slightly abrasive wear of the hard compound layer, thus the wear rate was very low.

To further investigate the fatigue failure of the TS sample after the inclined sliding test of 500 cycles, the sample was sliced along the wear track. After mounting and polishing, the sample was released from the epoxy mounting material. The sample was examined using the SEM in a BSE mode. During the observation, the sample was tilted by 45° so that the cross-section and the worn surface can be imaged simultaneously, as presented in Figure 4.13.

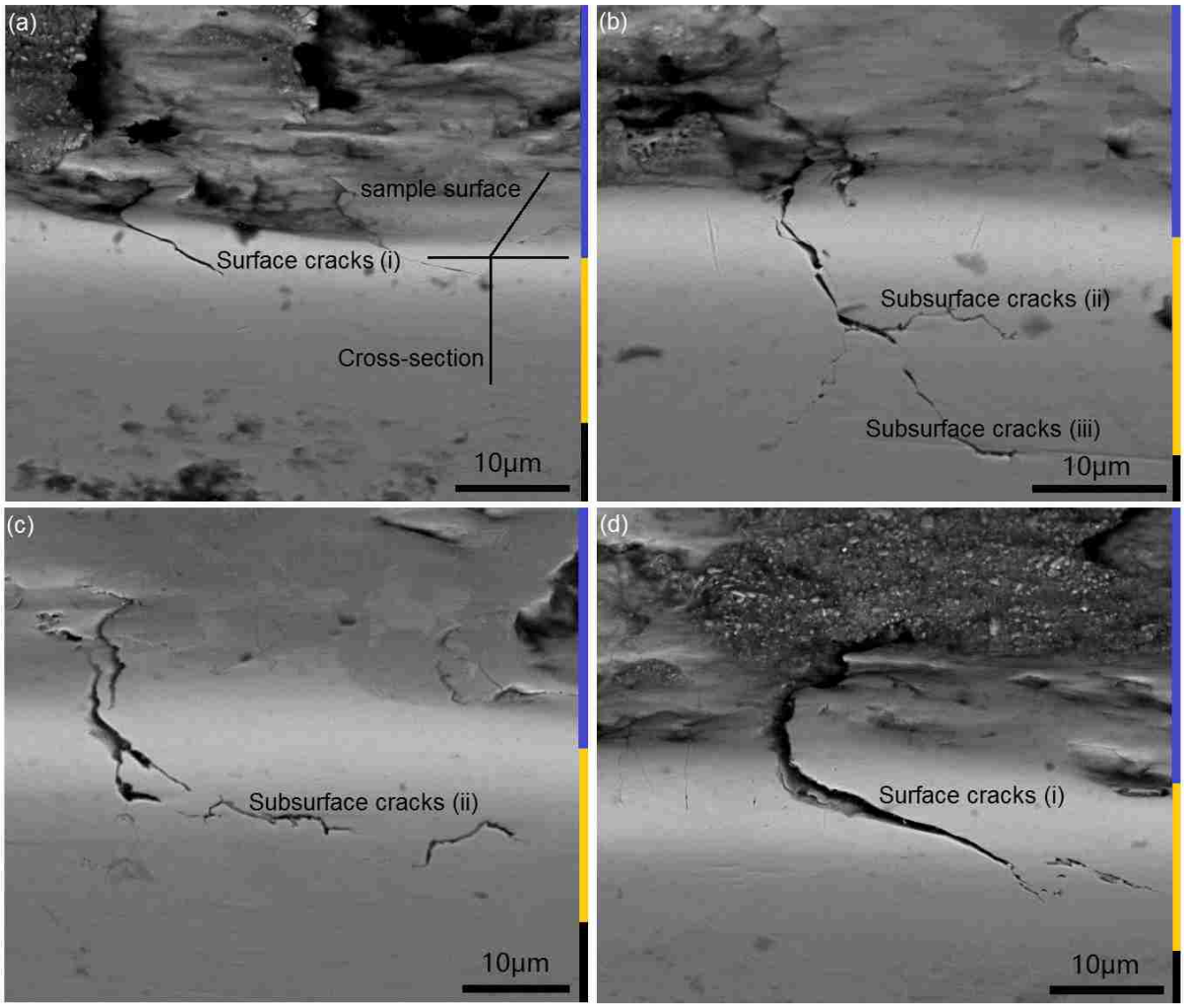


Figure 4.13 45º-tilted SEM observations on cut TS sample after 500 test cycles: (a) head area; (b) and (c) middle area; (d) tail area; the blue, yellow, and black bars on the right side represent the sample surface, the compound layer, and the diffusion zone, respectively.

In Figure 4.13, the upper part of the picture shows the worn surface, and the bottom part shows the sectional areas of the compound layer and the diffusion zone. Three kinds of cracks below the surface can be distinguished: (i) surface fatigue cracks initiated from the surface as shown in Figure 4.13 (a)–(d), where all the fatigue cracks propagated obliquely instead of along the vertical direction; (ii) subsurface cracks initiated within the compound layer, as shown in Figure 4.13 (d), and (iii) subsurface cracks initiated at the interface between the compound layer

and the diffusion zone, as shown in Figure 4.13 (b) and 4.13 (d). All the subsurface cracks seemingly propagated along a horizontal direction. During the inclined sliding tests, the sample was subjected to a very high contact pressure. The elastic modulus of the compound layer and diffusion zone were significantly different (295.8 GPa for the compound layer and 234.3 GPa at the depth of 30 μm for the diffusion zone). Thus, the corresponding strains were also significantly different, which may lead to bending of the compound layer. The bending effect induced a high normal stress $\sigma_n$ and a high tangential stress $\sigma_{t1}$ at the area near the contact center. Another tangential stress $\sigma_{t2}$ was caused by the friction force during the sliding against the SAE 52100 steel ball. The surface cracks were initiated by the tangential stresses. And then, the tips of the cracks were subjected to both tangential stress as well as normal stress. Therefore, the surface cracks propagated along an oblique direction. Moreover, the high normal stress led to the initiation and propagation of subsurface cracks. When the obliquely propagated surface cracks and the subsurface cracks connected with each other and formed a network, the compound layer chipped or peeled off.

On the contrary, as shown in Figure 4.5 (a) and Table 4.1, the diffusion zone of the TI sample was hard enough to support the compound layer on its surface sufficiently and it had an elastic modulus which was to that of the compound layer (298.8 GPa for the compound layer and 265.8 GPa at the depth of 30 μm for the diffusion zone). When the sample was subjected to high pressure, the difference in the corresponding strains between the compound layer and diffusion zone was negligible. The stresses caused by the bending effect of the compound layer were not large enough to initiate the subsurface cracks. Therefore, even though the surface cracks formed, crack networks did not form. The compound layer would not be chipped off during the test. The wear behavior of the TI sample was similar to that evaluated by the previous POD sliding tests.

Figure 4.14 schematically illustrates how the chipping and peeling could occur. After initiated by the cyclic motion and tangential stress, i.e., tensile stresses behind the sliding ball, all surface fatigue cracks propagated along a right-inclined direction (the steel ball slides from right to left). The subsurface cracks initiated and propagated due to the normal stresses caused by the bending effect within the compound layer and at the interface between the compound layer and the diffusion zone. When surface fatigue cracks connected with the subsurface cracks within the compound layer, the chipping occurred; when fatigue cracks connected with subsurface cracks at the interface, the larger peeling occurred. It was supposed to form edges I and III after chipping/peeling, as labeled in Figure 4.14. However, after the chipping and peeling, the area of the compound layer highlighted in a yellow color in Figure 4.14, could not bear the normal pressure of the steel ball on the sample surface and was broken down from the sample surface soon after the chipping and peeling. Therefore, only edges I and II could be observed after experiments.

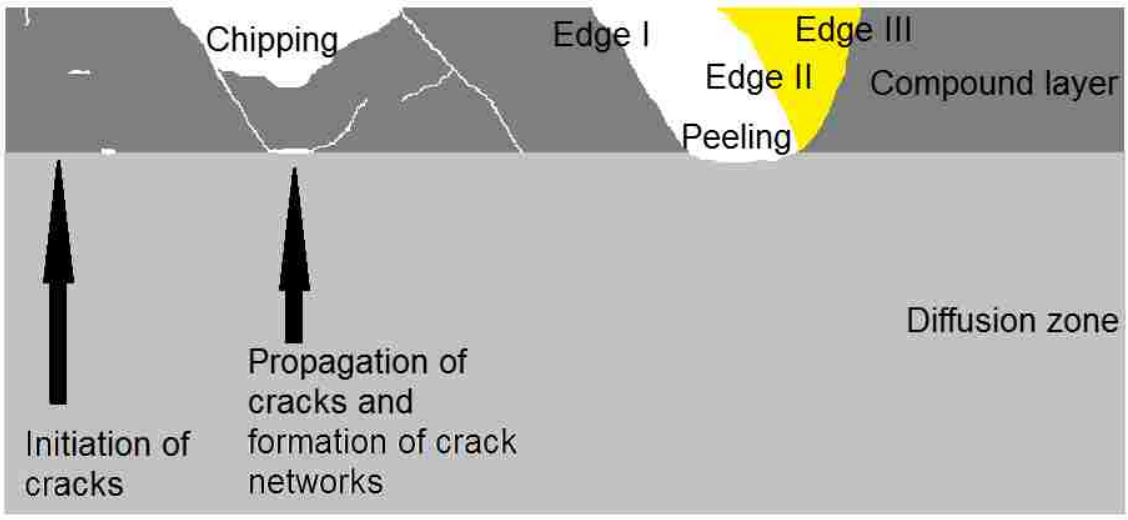


Figure 4.14 Schematic illustration of cracks initiation and propagation, chipping, and peeling of compound layer of TS sample.

It is noticed that the wear behaviors of the case-hardened layers under high-stressed inclined sliding were significantly different with those under pin-on-disk sliding. This phenomenon is due the two different apparatuses work in different regimes of sliding energy density as well as contact stress. As for the current experiments, during each cycle of the POD sliding tests, the sliding energy densities were about 0.004 J/mm$^2$ for the TI sample and 0.007 J/mm$^2$ for the TS sample. Fatigue cracks cannot initiate under such a low sliding energy density. On the other hand, when using the friction coefficients obtained from the POD sliding tests in the calculation for the inclined sliding tests, the ranges of the estimated sliding energy density of each cycle were 0.12-0.26 J/mm$^2$ for the TI sample and 0.21-0.46 J/mm$^2$ for the TS sample, which is comparable to the simulation results (up to 0.4 J/mm$^2$) and high enough for the initiation and propagation of fatigue cracks after a certain cycle of test. The results of the present study may be applied for the prediction of and protection against surface fatigue failure of metallurgical coatings on mechanical components, such as gear teeth, stamping dies, and so on. Moreover, the maximum contact stress during the inclined sliding tests could reach 3.9 GPa, which is much higher than 0.9 GPa during POD wear tests. The higher contact stress would promote the initiation and propagation of fatigue cracks by bending effect of the surface layer.

### 4.2.3 Summaries

During POD (normal) sliding tests, both plasma-nitrided ductile iron and cast steel samples mainly showed mild abrasive wear, polishing, and materials transferring on the surfaces. No surface fatigue cracking was observed. The wear resistance was seemingly controlled by the surface hardness and coefficient of friction.

Fatigue cracking was only observed during inclined sliding wear tests. This is due to the greatly higher contact stress and sliding energy density per cycle compared with POD tests.

During the inclined sliding test on the nitrided iron sample, a few surface fatigue cracks were formed. Even though, the compound layer was still attached to the diffusion zone and no chipping was observed. The wear was still characterized by abrasive wear and polishing, as well as material transfer and pile-up on sites of the surface where the graphite was originally located. On the contrary, the nitrided steel sample showed not only numerous fatigue cracks but also large areas of chipping and peeling.

The present study of failure mechanisms of nitrided cast iron and steel under high-stressed inclined sliding conditions shows that the wear/fatigue failure resistance relies not only on the surface hardness but also on the degrading of hardness and elastic modulus. High gradients of hardness and the elastic modulus would result in surface and subsurface fatigue cracking and accelerate the failure as demonstrated in the inclined sliding tests.

# Chapter 5: Elevated temperature effect on surface failure behavior of duplex treatment (W-doped CrN coating on nitrided H13 steel) under inclined impact-sliding wear test

In this chapter, W-doped CrN coatings were applied on plasma nitrided H13 steel samples using a physical vapor deposition process. A newly developed high temperature inclined impact-sliding wear tester was used to evaluate the coatings' wear behaviors under inclined sliding conditions against M50 high-speed steel balls at room temperature and 400 °C, respectively. Surface profilometer, scanning electron microscope (SEM), energy-dispersive X-ray spectroscopy (EDS), and X-ray photoelectron spectroscopy (XPS) were utilized to analyze the wear tracks. It was found that the coating performed better at elevated temperature; at a certain test load and number of cycles the coating was totally worn off at room temperature while remained unbroken at 400°C. SEM and EDS analysis revealed that the combined effect of surface fatigue cracking of the coating and materials transferring of the steel ball caused severe adhesive failure of the coating surface at room temperature. XPS analysis indicated the top surface layer (about 3-4nm) of the coating was oxidized at 400°C and formed a $Cr_2O_3$ protective film, which could reduce the adhesion between the coating and the steel ball. The in-situ formation of the thin $Cr_2O_3$ protective layer likely led to the change of wear mechanisms from severe adhesive failure to mild abrasive wear.

## 5.1 Inclined impact-sliding wear tests at room and elevated temperature

Before the inclined impact-sliding wear tests, the hardness and elastic modulus of the duplex treatment were measured, the results are summarized in Table 5.1.

Table 5.1 Mechanical properties of the coated system.

| | | |
|---|---|---|
| CrN coating layer | Thickness, μm | 6 |
| | Hardness, GPa | 22 |
| | Elastic modulus, GPa | 300 |
| Nitriding case | Thickness, μm | 120 |
| | Hardness, $HV_{0.2}$ | 1200 |
| Substrate | Hardness, HRC | 52 |

Figure 5.1 is the surface profiles measured at the center of the wear tracks after 2000 cycles of the test. The maximum wear track depth of the sample tested at 400°C was less than 2μm, indicating the coating (the coating thickness ~6μm) was not penetrated yet. On the other hand, the maximum wear track depth of the sample tested at room temperature was about 12μm, about twice as the thickness of the coating, showing the penetration of the coating during the test.

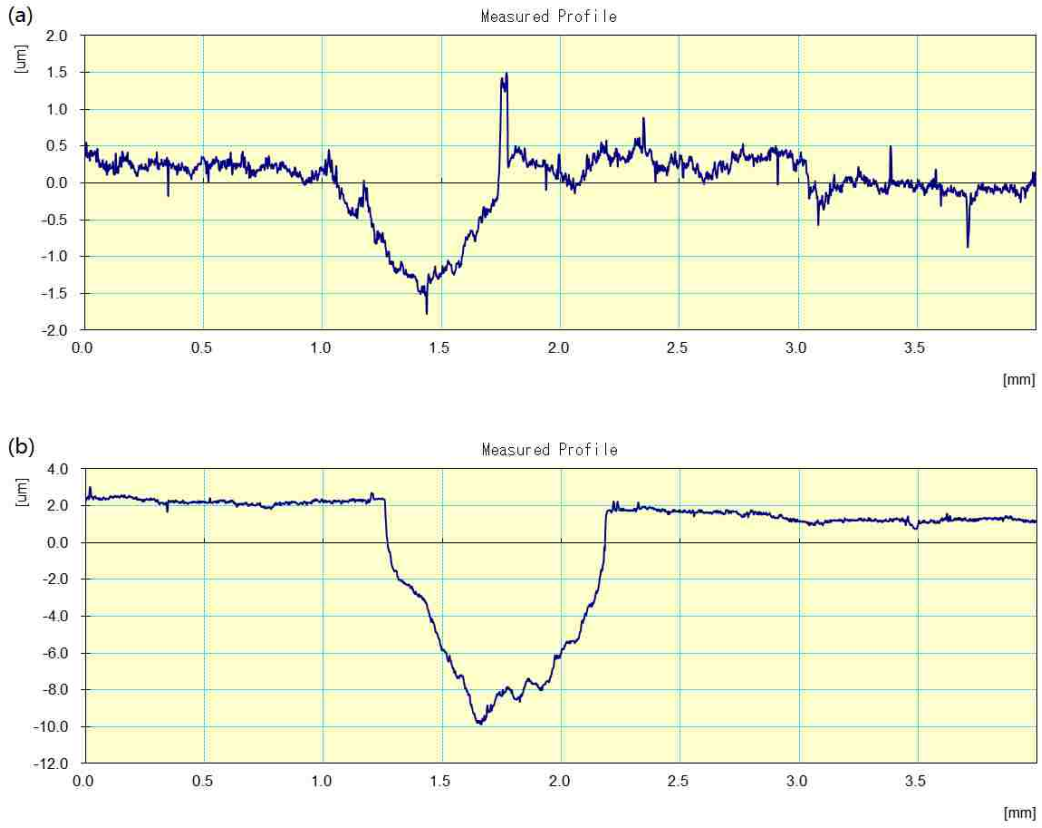


Figure 5.1 Measured profiles at the centre of the wear track; (a) tested at 400°C, and (b) tested at room temperature.

To get a whole picture of the wear behavior of the CrN coatings at room temperature and 400°C; the wear tracks were observed using SEM (13KV, MIX mode). Figures 5.2 and 5.3 show the SEM images of the wear tracks of the samples tested at room temperature and 400°C for 2000 cycles, respectively.

As demonstrated in Figure 5.2, the coating in the contact area was almost worn away at room temperature after 2000 cycles of the test. EDS mapping shows the peeling of the coating and the exposure of the substrate. This phenomenon indicates that the wear resistance of the W-doped CrN coating was not excellent when sliding against M50 steel balls under extremely high contact

stress at room temperature. It is noted that during the previous study on the wear behavior of CrN coatings (processing parameters were the same as the present study but without W doping), the coatings were not severely peeled off (only some small areas of peeling was observed) even after 5000 cycles of the test [87]. The difference of the wear behaviors reminds that the W-doped CrN coating used in this study may have a lower bonding strength to the substrate. The processing parameters may need to be modified for the optimization of the interfacial bonding strength of the W-doped CrN coating.

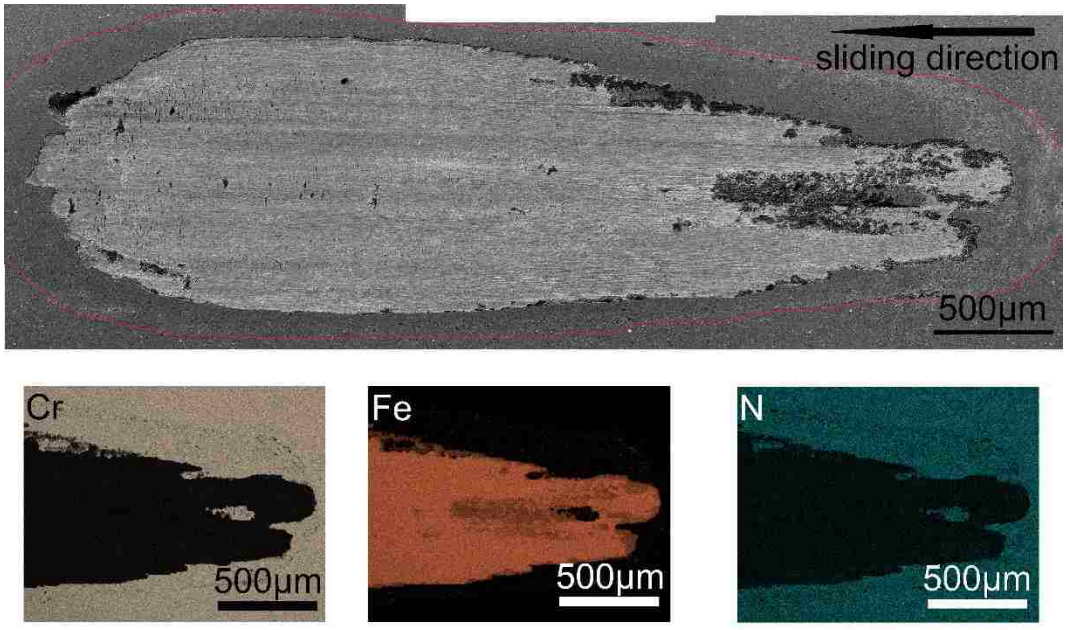


Figure 5.2 The overview of the wear track of the CrN coating tested at room temperature for 2000 cycles. The red curve marked the boundary of the wear track, and the white arrow indicated the sliding direction. Inserts were the EDS mapping images at the head area of the wear track, showing the distribution of Cr and Fe.

On the other hand, as shown in Figure 5.3 (a), the coating in the wear track tested at 400°C was still in good condition. Although some small areas of wear debris pile-up and a few surface fatigue cracks could be found at the tail area of the coating, no severe chipping or peeling was

revealed. Figure 5.3 (b)-(e) shows the detailed morphology at different positions (corresponding to point B- head area, C- middle area, and D&E- tail area) of the wear track. As shown in Figure 5.3 (b)-(d), numerous small surface fatigue cracks could only be observed at the higher magnification. The EDS point analysis on the piled wear debris presents a high content of Fe and O, indicating it was the transferring and oxidation of materials from the M50 steel ball. In Figure 5.3 (e), EDS point analysis suggests a high content of Fe and N which was similar to the chemical composition of a typical nitriding case layer, indicating the peeling of the coating and exposure of the substrate (plasma nitrided H13 steel). Point E is the only site of peeling found inside the whole wear track; this means that the W-doped CrN coating could have a high wear resistance at 400°C when sliding against M50 steel ball even under such an extremely high contact stress.

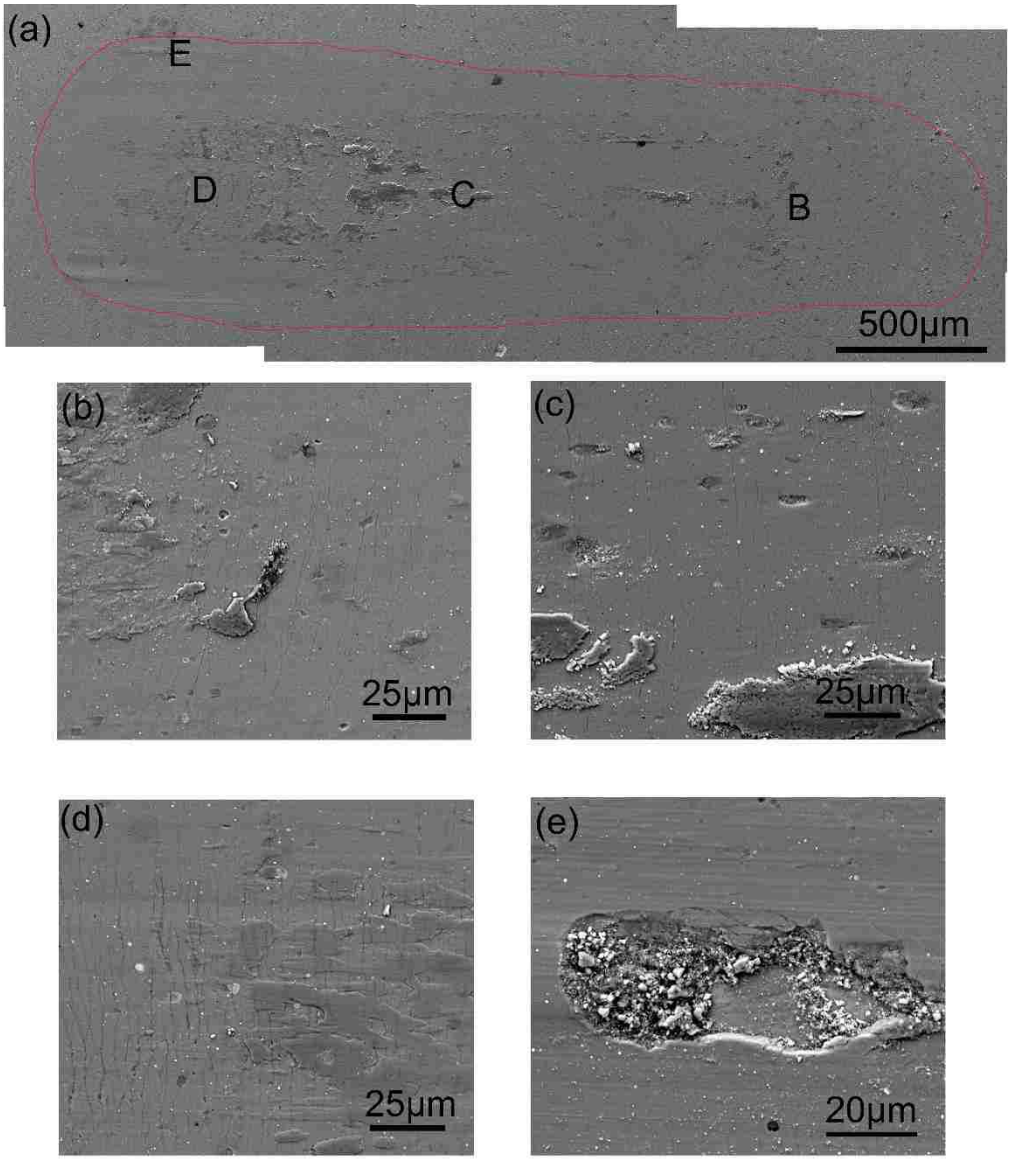


Figure 5.3 SEM images of the wear track of the CrN coating tested at 400°C for 2000 cycles; (a) overview of the wear track; (b), (c), (d), and (e) showed the detailed morphologies at a higher magnification corresponding to point B, C, D, and E in (a). The red curve marked the boundary of the wear track.

### 5.2 Coating failure mechanisms

The test results above demonstrate that the elevated temperature would enhance wear resistance of the W-doped CrN coating at the given testing condition (i.e., sliding against M50

steel ball under extremely high contact stresses). The wear mechanism at 400°C and 2000 cycles was mainly the polishing of the coating surface with tiny surface cracking and slight materials transferring from the steel ball. However, 2000 cycles were too much for the coating tested at room temperature, since the coating was almost entirely gone after the test and it was not able to figure out the failure mechanism. In fact, repeated tests showed that the W-doped CrN coating appeared to have damages at the test cycles as low as hundreds. Therefore, an extra test of 100 cycles was carried out here for better investigation of the coating's failure behavior. The SEM images of corresponding wear track were presented in Figure 5.4.

As shown in Figure 5.4 (a), the coating still exhibited a large degree of chipping and peeling after 100 cycles of the test at room temperature. At the edge of the wear track, large areas of materials transferring and adhesion from the steel ball, i.e. the bright area along the edge of the wear track, could be found. Figure 5.4 (b)-(e) show the detailed morphologies corresponding to point B- residual coating in the head area, points C&D- edge, and point E- tail area of the wear track. The white stars marked the positions of EDS point analysis, and the inserts showed the corresponding EDS spectra. The results were summarized in Table 5.2. From Table 5.2, it is noted that the materials from the M50 steel ball were transferred to the coating surface.

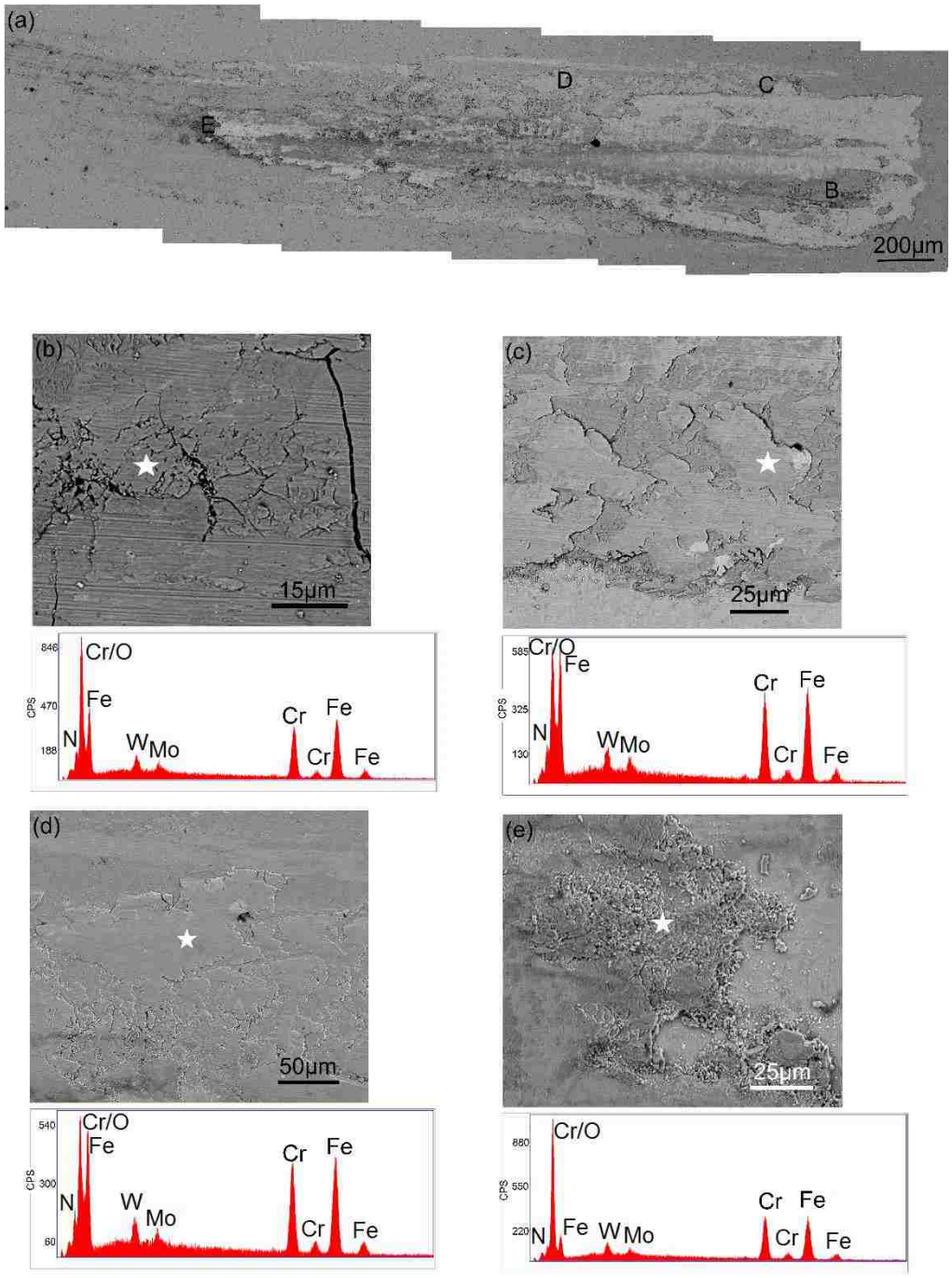


Figure 5.4 SEM images of the wear track of the CrN coating tested at room temperature for 100 cycles; (a) overview of the wear track; (b), (c), (d), and (e) showed the detailed morphologies at a higher magnification corresponding to point B, C, D, and E in (a). White stars marked the EDS analysis positions. Inserts are the corresponding EDS spectra.

Table 5.2 EDS point analysis on the wear debris of the sample tested at room temperature for 100 cycles.

| EDS spot | Element composition (wt.%/at.%) | | | | |
|---|---|---|---|---|---|
| | Cr | N | Fe | O | Balanced |
| (b) | 24/17 | 6/17 | 53/35 | 13/30 | Balanced |
| (c) | 25/18 | 5/14 | 53/35 | 8/18 | Balanced |
| (d) | 26/19 | 6/16 | 54/37 | 8/19 | Balanced |
| (e) | 22/13 | 7/15 | 44/24 | 22/40 | Balanced |

* Based on the nature of this study, only the contents of Cr, N, Fe, and O are reported here.

Figure 5.5 shows the SEM image of the wear scar of the M50 steel ball after 100 cycles of the test at room temperature. EDS mapping images illustrate the distribution of Cr, N, Fe, and O on the worn surface of the steel ball. It is evident that more than half of the worn area showed the existence of Cr and N. The average chemical composition of the blue area was 19 at.% Cr, 14 at.% N, 29 at.% Fe, and 26 at.% O. These values were in good consistency with the chemical composition of the transferred materials on the CrN coating surface. This phenomenon indicates that during the test, the worn surfaces of the coating and transferred materials from the steel ball were bonded and mixed together under the extremely high contact stress; and then the mixture could be transferred back to the steel ball surface.

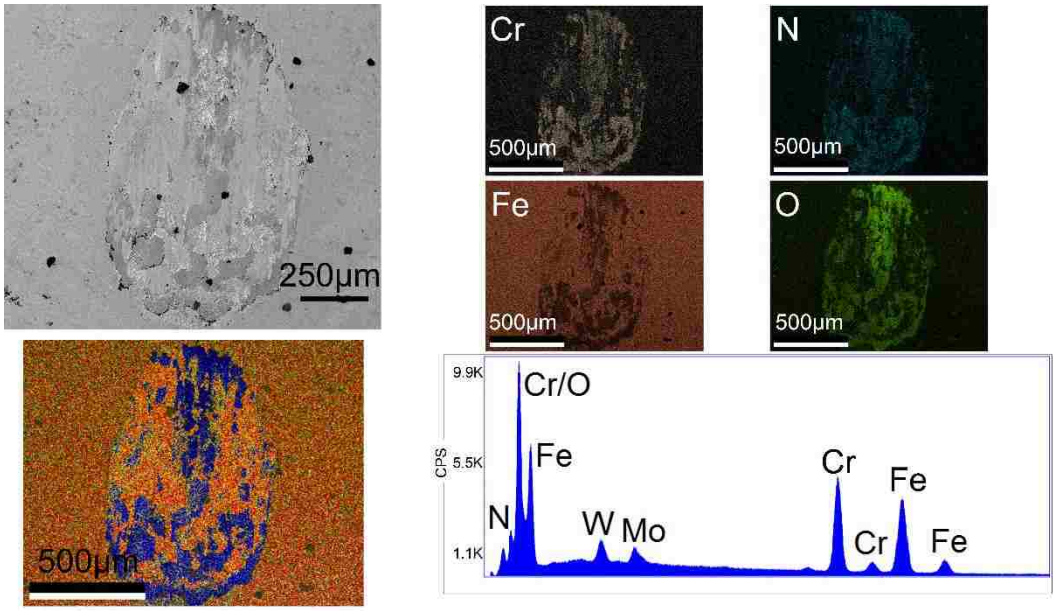


Figure 5.5 SEM images of the wear scar on the M50 steel ball after 100 cycles test at room temperature. Inserts are the live map (with EDS spectra) and elements map.

While relative movement occurred, large shear and normal stresses were introduced to the coating through the mixture bonding layer. Depending on the strength of the coating, the bonding strength between the coating and the substrate, as well as the strength of this mixture bonding layer, chipping and peeling of the coating from the substrate or tearing materials from the steel ball could occur. In the present study, surface fatigue cracks formed in the coating due to cyclic motion of the steel ball and extremely high contact stress on its surface, as shown in Figure 5.6. These cracks reduced the strength of the coating and may also influence the bonding strength between the coating and substrate if they propagated to the interface. Therefore, chipping and peeling of the coating from the substrate was likely to occur during the test.

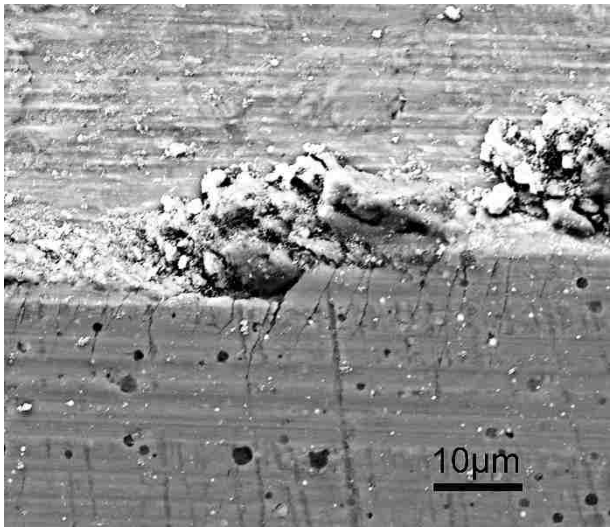


Figure 5.6 SEM image at the edge of the chipping area without materials transferring, showing the existence of surface fatigue cracking (tips). The sample was tested at room temperature for 100 cycles.

### 5.3 The effects of elevated temperature

It has been reported in [76] that the hardness and elastic modulus of the CrN coating did not decrease before 500°C. In our experiment, the tests were performed at 400°C with a variation no more than 5 degrees (calibrated via a K-type thermocouple, Omega Inc.). Thus, the mechanical properties of the CrN coating should have insignificant changes. The effect of elevated temperature on improving the coating's wear resistance should rely on the possible alternation of surface properties. To figure out the effect of elevated temperature on the evolution of coating's surface, XPS analyses were carried on the as-received sample, and the 400°C tested sample, respectively. Away from the wear track, survey scan analyses were carried out with an analysis area of 300 x 700 microns and a pass energy of 160 eV, and then high-resolution analyses were carried out with a pass energy of 20 eV. Inside the wear track, analysis area with a size of 400 x 400 microns was used. Spectra have been recorded and corrected to the main line of the carbon 1s spectrum (adventitious carbon) set to 284.8 eV. Spectra were analyzed using CasaXPS

software (version 2.3.14). The fitted Cr 2p peak spectra and W 4f peak spectra measured on the as-received sample and the tested sample (inside and outside the wear track) were presented in Figure 5.7.

As shown in Figure 5.7 (a)-(c), the fitted W 4f peak spectra did not reveal a significant difference between the as-received sample and 400°C tested sample. The W on the top surfaces of both as-received sample and 400°C tested sample was oxidized, and the tungsten oxides consist of $WO_2$ and $WO_3$. The ratio of $WO_2/WO_3$ was about 3 for the as-received sample. For the sample test at 400°C, the ratio was 2.16 inside the wear track and 1.85 outside the wear track, respectively. The decreased $WO_2/WO_3$ ratio at elevated temperature implied the further oxidation of the tungsten at elevated temperature. However, the change only in the $WO_2/WO_3$ ratio between the as-received sample and the 400°C tested sample would not be significant, particular when the total content of W in the present coating was merely about 1.8 at.%. Therefore, the tungsten oxides might not play the key role in improving the wear resistance at 400°C.

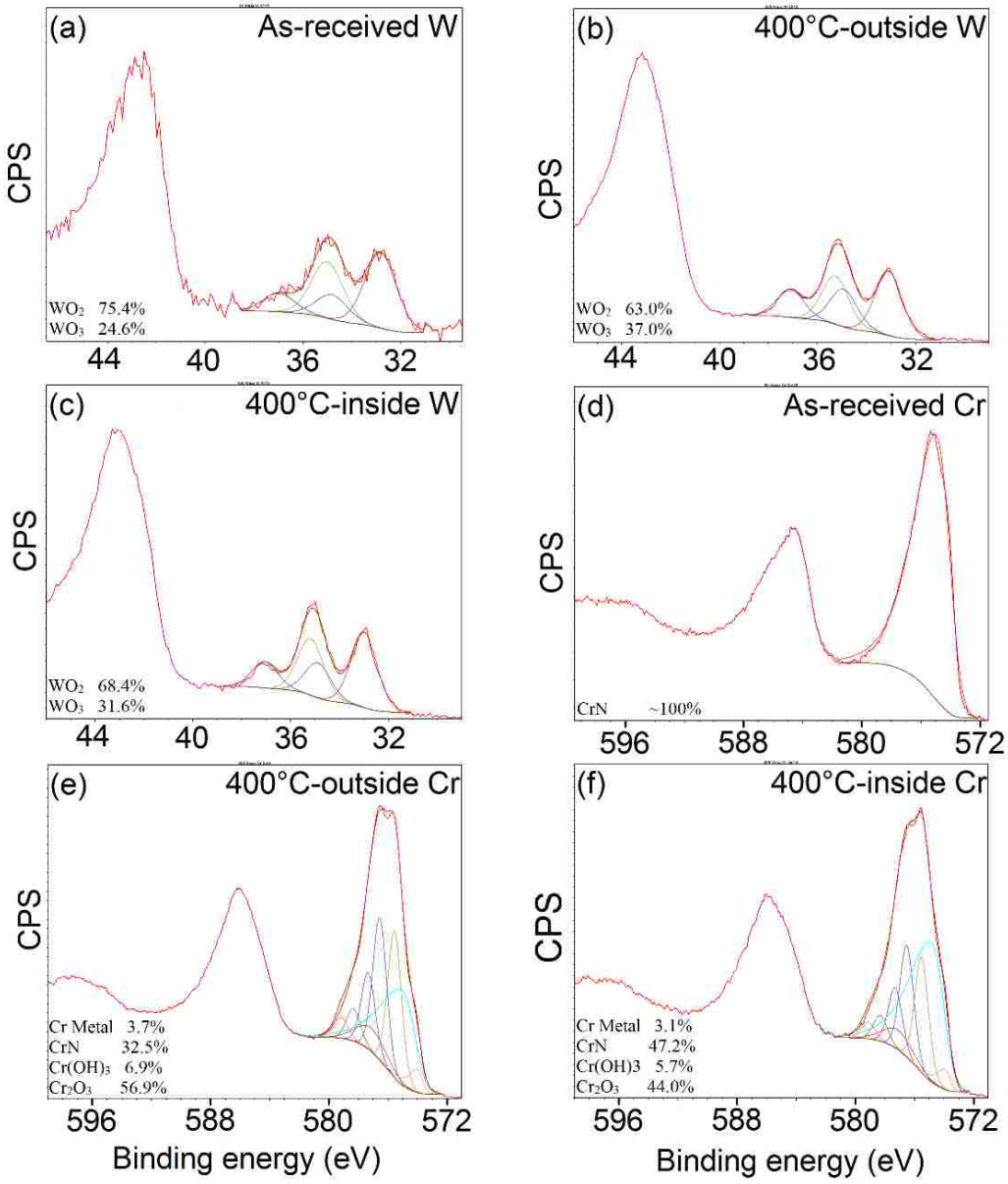


Figure 5.7 Fitted W 4f peak spectra measured on (a) as-received coating surface; and 400°C tested sample surface at (b) area away from the wear track, and (c) area inside the wear track; and fitted Cr 2p peak spectra measured on (d) as-received coating surface; and 400°C tested sample surface at (e) area away from the wear track, and (f) area inside the wear track. The oxidation of Cr at 400°C was cleared demonstrated.

In contract with the W 4f peak spectra, the fitted Cr 2p peak spectra revealed a significant difference between the as-received sample and 400°C tested sample. As shown in Figure 5.7 (d),

the as-received coating mainly consists of CrN while $Cr_2O_3$ was not detected, indicating that the CrN was not oxidized at room temperature. On the contrary, about 57% of detected Cr was oxidized and converted into $Cr_2O_3$ at the position away from the wear track, as shown in Figure 5.7 (e). Inside the wear track, about 44% of detected Cr was converted into $Cr_2O_3$, as shown in Figure 5.7 (f). The slight difference in the $Cr_2O_3$ contents between the areas inside and outside the wear track indicates the wear loss of $Cr_2O_3$. Plus the SEM observation above, one of the coating wear mechanisms was the polishing of the coating surface.

From the XPS analysis, it is evident that the oxidation of Cr at the surface contributed to the improved wear resistance at elevated temperature. The oxidation converted Cr at the surface into a compact $Cr_2O_3$ layer, which could effectively reduce the adhesion between the coating surface and the steel ball (probably by prohibiting the diffusion of iron and oxygen into the CrN coating). Therefore, the wear mechanism changed from severe adhesive wear (galling) at room temperature into mild abrasive wear at 400°C. After a few cycles, this $Cr_2O_3$ layer was worn away, and the CrN coating was exposed to the air again. Then, during the heating period of the next cycle, a new $Cr_2O_3$ layer formed on the worn surface again. The in-situ formation of the $Cr_2O_3$ layer, which could effectively protect the CrN coating from severe adhesive wear, provided superior wear resistance of CrN coating at elevated temperatures.

To verify this explanation, two additional experiments were carried. The first one was to replace the M50 steel ball with alumina ball at room temperature, i.e. to reduce the adhesion between the coating and the indent surfaces. Despite the alumina ball had a higher hardness and elastic modulus, which could lead to the lower contact area and thus higher contact stress, the coatings were still in good condition even after 2000 cycles of the test. No materials transferring or adhesion from the impact indent (alumina ball) was found. No chipping or peeling was

observed either. Another additional experiment was to test the pre-oxidized sample (the sample tested at 400°C) at room temperature with an M50 steel ball. The coating failure initiation was determined to occur after 120 cycles, which were 20 cycles later than the as-received sample tested at room temperature. The delayed initiation of failure could be attributed to the benefit of the thin $Cr_2O_3$ layer. After the oxide layer was worn off, no additional $Cr_2O_3$ layer could be re-generated, different from the test at the elevated temperature where the thin oxide layer can be in-situ formed during the progress of the test. These two additional experiments clearly pointed out that the in-situ formation of the $Cr_2O_3$ layer on the coating surface played a key role in improving the wear resistance at the elevated temperature.

From above analysis, it suggests that elevated temperature prompted the oxidation of Cr and formation of a thin $Cr_2O_3$ layer. The in-situ formation of the $Cr_2O_3$ layer could effectively reduce the adhesion of steel ball surface to the coating surface under extremely high contact stress. Thus, the wear mechanism changed from severe adhesive wear (galling) at room temperature into mild abrasive wear at elevated temperature (400°C). The severe adhesion-induced failure of the CrN coating at room temperature when sliding against M50 steel ball indicates that the bonding strength between the coating and the substrate was not excellent. For the application of this coating at room temperature under extremely high contact stresses, the use of W for reduction of adhesion between the contact surfaces should be a good concept, since addition of a solid lubricant (such as $MoS_2$ and $WS_2$, with a necessary amount of weight percentage) into a hard coating may be promising for improving the coating's wear resistance under the extreme conditions. However, the coating deposition parameters need to be optimized to achieve an as high as possible bonding strength between the coating and the substrate. Although the tested W-doped CrN coating was not very successful in the test at room temperature, the coating

performed well at elevated temperatures; the latter was due to the in-situ formation of Cr oxide not because of W oxide. Modification of the W-doped CrN coating with an excellent bonding strength is still undertaken.

### 5.4 Summaries

A plasma nitriding and PVD coating (duplex treatment) were applied on H13 steel. The hardness of the W-doped CrN coating and the nitriding case was 22 GPa and 1200 HV0.2, respectively.

The inclined sliding wear tests of the coated samples against M50 steel balls under the contact stress up to 3.4 GPa showed a much-improved wear resistance at the elevated temperature (400˚C), compared to results shown at room temperature.

SEM/EDS analysis indicated that the coating was subjected to severe adhesive wear (galling) at room temperature due to the strong adhesion between the coating and the steel ball. XPS analysis demonstrates that W oxides were formed at both room and elevated temperatures. Cr oxides were formed only at elevated temperature, and the thin Cr oxide layer was believed to be re-generated when the layer started to be thinned during the test wear progress. The in-situ formation of the thin Cr2O3 layer reduced the adhesion and thus changed the wear mechanism into mild abrasive wear.

To improve the wear property of the W-doped CrN coating at room temperature, a higher amount of W and better interfacial bonding strength would be needed when the coating intends to be used in applications of extremely high contact stress conditions.

# Chapter 6: Conclusions and future work

The hot stamping die materials were evaluated by the inclined impact-sliding wear tests at both room and elevated temperatures. In order to figure out the wear mechanisms, the wear tracks were analysed by the surface profilometer, scanning electron microscope (SEM), energy-dispersive X-ray spectroscopy (EDS) and X-ray photoelectron spectroscopy (XPS). Based on the test results and characterization of the wear tracks, the following conclusions and future works are drawing.

## 6.1 Conclusions

Inclined impact-sliding wear tests were performed on the hot stamping die materials (nitrided cast iron/steels and duplex treatment on the H13 hot work steel). Surface profilometer, scanning electron microscope (SEM), energy-dispersive X-ray spectroscopy (EDS) and X-ray photoelectron spectroscopy (XPS) were utilized to characterize the wear and failure behaviors of the samples under extreme conditions. Based on this classification, how the die material reacts under inclined impact-sliding tests, such as surface fatigue cracking, chipping and peeling or just abrasive wear of the surface was determined. It was expecting that the results can then be applied for improving the design and protection of stamping die materials.

Nitriding was performed on the cast irons (NAAMS-D6510) and cast steels (NAAMS-S0050A) by plasma nitriding, fluidized bed nitriding and pulsed plasma diffusion (PPD) nitriding, respectively. During POD (normal) sliding tests, both nitrided ductile iron and cast steel samples mainly showed mild abrasive wear, polishing, and materials transferring on the surfaces. No surface fatigue cracking was observed. The wear resistance was seemingly controlled by the surface hardness and coefficient of friction.

Fatigue cracking was only observed during inclined sliding wear tests. This is due to the greatly higher contact stress and sliding energy density per cycle compared with POD tests. During the inclined sliding test on the nitrided iron sample, a few surface fatigue cracks were formed. Even though, the compound layer was still attached to the diffusion zone and no chipping was observed. The wear was still characterized by abrasive wear and polishing, as well as material transfer and pile-up on sites of the surface where the graphite was originally located. On the contrary, the nitrided steel sample showed not only numerous fatigue cracks but also large areas of chipping and peeling. The failure resistance of nitrided cast iron and steel under high-stressed inclined sliding conditions relies not only on the surface hardness but also on the hardness profile and elastic modulus. High gradients of hardness and the elastic modulus would result in surface and subsurface fatigue cracking and accelerate the failure as demonstrated in the inclined sliding tests. The PPD nitrided cast iron, which had the highest surface hardness and relatively low hardness gradient, had the highest failure resistance.

A plasma nitriding and PVD coating (duplex treatment) were applied on H13 steel. The hardness of the W-doped CrN coating and the nitriding case was 22 GPa and 1200 HV0.2, respectively. Inclined cyclic impact-sliding wear tests of 2000 cycles were carried on the samples at both room temperature and 400˚C.

The inclined impact-sliding wear tests showed a much-improved wear resistance at the elevated temperature (400˚C), compared to results shown at room temperature. SEM/EDS analysis indicated that the coating was subjected to severe adhesive wear (galling) at room temperature due to the strong adhesion between the coating and the steel ball. Numerous fatigue cracks, severe materials transferring and large area chipping/peeling of the CrN coating characterized the morphology of the wear tracks which were tested at room temperature.

XPS analysis demonstrates that W oxides were formed at both room and elevated temperatures. Thus, considering the small amount of total W doping, the influence of W oxides should not be large enough to cause such a big difference between the coating's performance at room temperature and 400˚C. On the other hand, Cr oxides were formed only at elevated temperature. At 400˚C, about half of the detected Cr existed in the form of $Cr_2O_3$. The thin Cr oxide layer was believed to be re-generated when the layer started to be thinned during the test wear progress. The in-situ formation of the thin $Cr_2O_3$ layer reduced the adhesion and thus changed the wear mechanism into mild abrasive wear. To improve the wear property of the W-doped CrN coating at room temperature, a higher amount of W and better interfacial bonding strength would be needed when the coating intends to be used in applications of extremely high contact stress conditions.

### 6.2 Future work

The 3D-load cell could be added on the inclined impact-sliding wear tester to monitor and record the dynamic loads during the tests. The data could be used for calculation of normalized COF (coefficient of friction) and FEM simulation of the process. FEM simulation of the tests is another interesting research interest. By these approaches, the wear and failure mechanisms of coated systems under impact-sliding wear conditions can be understood in a greater detail. To sum up, the methodology used in this work not only can be carried out for evaluating the stamping die materials, but also offer a promising approach to evaluate other materials work under conditions which involve impacting and sliding simultaneously.

For the failure of W-doped CrN coating, additional experiments could be conducted on the samples with different level of W-doping to figure out the actual influence of the W on the coating's performance.

# REFERENCES


[1] Patent GB 1490535, 1977. Manufacturing a hardened steel article, Norrbottens Jaernverk AB.

[2] Aspacher, J., Forming hardening concepts, 2008. In: 1st International Conference on Hot Sheet Metal Forming of High-Performance Steel, Kassel, Germany, pp 77–81.

[3] Åkerström, P., Wikman, B., Oldenburg, M., Material parameter estimation for boron steel from simultaneous cooling and compression experiments. Modelling and Simulation in Materials Science and Engineering, 2005, 13, pp 1291–1308.

[4] Åkerström, P., Bergman, G., Oldenburg, M., Numerical implementation of a constitutive model for simulation of hot stamping. Materials Science and Engineering, 2007, 15, pp 105–119.

[5] Bariani, P.F., Bruschi, S., Ghiotti, A., Tureta, A., Testing formability in the hot stamping of HSS. CIRP Annals—Manufacturing Technology, 2008, 57, pp 265–268.

[6] Behrens, B.A., Hübner, S., Demir, M., Conductive heating system for hot sheet metal forming, 2008. In: 1st International Conference on Hot Sheet Metal Forming of High-Performance Steel, Kassel, Germany, pp 63–68.

[7] Bergman, G., Oldenburg, M., A finite element model for thermo-mechanical analysis of sheet-metal forming. International Journal for Numerical Methods in Engineering, 20004, 59, pp 1167–1186.

[8] Chastel, Y., Dahan, Y., Massoni, E., Duroux, P., Wilsius, J., Hein, P., Formability of quenchable steels in hot stamping, 2008. In: The 9th International Conference on Technology of Plasticity, ICTP, Gyeongiu, Korea, pp 678–683.

[9] Erhardt, R., Böke, J., Industrial application of hot forming press simulation, 2008. In: 1st International Conference on Hot Sheet Metal Forming of High-Performance Steel, Kassel, Germany, pp 83–88.

[10] Faderl, J., Manzenreiter, T., Radlmayr, M., Press hardening of hot-dip galvanized 22MnB5: a stable and reproducible process, 2008. In: 1st International Conference on Hot Sheet Metal Forming of High-Performance Steel, Kassel, Germany, pp 199–205.

[11] Faderl, J., Kolnberger, S., Kurz, T., Luckeneder, G., Martenreiter, T., Rosner, M., phs-ultraform®—continuous galvanizing meets press-hardening, 2009. In: 2nd International Conference on Hot Sheet Metal Forming of High-Performance Steel, Luleå, Sweden, pp 283–292.

[12] Forstner, K., Strobich, S., Buchmayr, B., Heat transfer during press hardening, 2007. International Deep Drawing Research Group IDDRG, Gyo″ r, Hungary, pp 609–613.

[13] Garcia Aranda, L., Chastel, Y., Fernández Pascual, J., Dal Negro, T., Experiments and simulation of hot stamping of quenchable steels. Advanced Technology of Plasticity, 2002, 2, pp 1135–1140.

[14] Dessain, Ch., Hein, P., Wilsius, J., Penazzi, L., Boher, Ch., Weikert, J., Experimental investigation of friction and wear in hot stamping of usibor 1500P, 2008. In: 1st International Conference on Hot Sheet Metal Forming of High-Performance Steel, Kassel, Germany, pp 217–227.

[15] Hardell, J., Prakash, B., High temperature friction and wear behavior of different tool steels during sliding against Al–Si-coated high strength steel. Tribology International 2008, 41 (7), pp 663–671.

[16] Mercedes-Benz 111 Series (1959 to 1968). [Image from “August 1959: Mercedes-Benz introduces the safety body”]. Retrieved from http://www.mercedesclass.net/?page_id=48

[17] Billur, E., Altan, T., Challenges in Forming Advanced High Strength Steels, Engineering Research Center for Net Shape Manufacturing (ERC/NSM), 2010, 9, pp 2-7

[18] AHSS 101: Evolving Use of Advanced High-Strength Steels for Automotive Applications, The Automotive Applications Council of the Steel Market Development Institute (SMDI).

[19] Future Steel Vehicle program report, Phase I - Executive Summary, World Auto Steel.

[20] Auto/Steel Partnership. “A Special Edition of AHSS Case Studies.” Advanced High-Strength Steel Applications: Design and Stamping Process Guidelines, 2011.

[21] McCallum, S. and Taylor, M., Upper and Lower Body Structure Design Strategies Implemented on the 2011 Chevrolet Volt, 2011. [Powerpoint presentation at Great Designs in Steel Seminar].

[22] Courtesy of Volkswagen.

[23] Lechler, J., Merklein, M., Geiger, M., Determination of thermal and mechanical material properties of ultra-high strength steels for hot stamping. Steel Research International, 2009, 79 (2), 98–104.

[24] Suehiro, M., Kusumi, K., Miyakoshi, T., Maki, J., Ohgami, M., Properties of aluminium-coated steels for hot-forming, 2003, Nippon Steel Technical Report No.88, pp 16–21.

[25] Lenze, F.J., Banik, J., Sikora, S., Applications of hot formed parts for body in white. International Deep Drawing Research Group IDDRG, 2008, pp 511–519.

[26] Kolleck, R., Aspacher, J., Veit, R., Efficienty of hot forming processes, 2009. In: 2nd International Conference on Hot Sheet Metal Forming of High-Performance Steel, Luleå, Sweden, pp 173–179.

[27] Kolleck, R., Veit, R., Merklein, M., Lechler, J., Geiger, M., Investigation on induction heating for hot stamping of boron alloyed steels. CIRP Annals—Manufacturing Technology 2009, 58, pp 275–278.

[28] Mori, K., Maki, S., Tanaka, Y., Warm and hot stamping of ultra-tensile strength steel sheets using resistance heating. CIRP Annals—Manufacturing Technology, 2009, 54 (1), pp 209–212.

[29] Kolleck, R., Veit, R., Hofmann, H., Lenze, F.J., Alternative heating concepts for hot sheet metal forming, 2008. In: 1st International Conference on Hot Sheet Metal Forming of High-Performance Steel, Kassel, Germany, pp 239–246.

[30] Karbasian, H., Tekkaya, A.E., A review on hot stamping. Journal of Materials Processing Technology, 2010, 210, pp 2103–2118.

[31] Merklein, M., Lechler, J., Determination of material and process characteristics for hot stamping processes of quenchable ultra-high strength steels with respect to a FE-based process design. SAE World Congress: Innovations in Steel and Applications of Advanced High Strength Steels for Automobile Structures, 2008, Paper No. 2008–0853.

[32] Naderi, M., Hot stamping of ultra-high strength steels. Doctoral Theses, RWTH Aachen, 2007.

[33] Friedrich, C., et al. "PVD Cr x N coatings for tribological application on piston rings." Surface and Coatings Technology, 1997, 97 (1): pp 661-668.

[34] Zlatanović, M., "Deposition of (Ti, Al) N coatings on plasma nitrided steel." Surface and Coatings Technology, 1991, 48 (1): pp 19-24.

[35] Van Stappen, M., Malliet, B., Stals, L., De Schepper, L., Roos, J.R., Celis, J.P., Characterization of TiN coatings deposited on plasma nitrided tool steel surfaces. Materials Science and Engineering: A, 1991, 140(0): pp 554-562.

[36] Smolik, J., Walkowicz, J., Tacikowski, J., Influence of the structure of the composite: 'nitrided layer/PVD coating' on the durability of tools for hot working. Surface and Coatings Technology, 2000, 125(1–3): pp 134-140.

[37] Wilson, A.D., Leyland, A., Matthews, A., A comparative study of the influence of plasma treatments, PVD coatings and ion implantation on the tribological performance of Ti–6Al–4V. Surface and Coatings Technology, 1999, 114(1): pp 70-80.

[38] Batista, J.C.A., Joseph, M.C., Godoy, C., Matthews, A., Micro-abrasion wear testing of PVD TiN coatings on untreated and plasma nitrided AISI H13 steel. Wear, 2001, 249(10–11): pp 971-979.

[39] Ma, S., Li, Y., Xu, K., The composite of nitrided steel of H13 and TiN coatings by plasma duplex treatment and the effect of pre-nitriding. Surface and Coatings Technology, 2001, 137(2–3): pp 116-121.

[40] Retrieved from: http://www.hcvacuum.com/node/61, July 07, 2017

[41] Vetter, J., Barbezat, G., Crummenauer, J., Avissar, J., Surface treatment selections for automotive applications. Surface and Coatings Technology, 2005, 200(5-6): pp 1962-1968.

[42] Bott, A. H., et al. "Pulsed-plasma-nitrided API 5L X-65 steel: hydrogen permeability and microstructural aspects." Journal of Physics D: Applied Physics, 1998, 31(24): pp 3469.

[43] Zhang, Z. L., Bell, T., "Structure and corrosion resistance of plasma nitrided stainless steel." Surface Engineering, 1985 1 (2): pp 131-136.

[44] "Thermal Spray as a Sputter Target Production Method." Glass Canada. Glass Canada Magazine, 31 Mar. 2009.

[45] Davis, J.R., Handbook of thermal spray technology, 2004, ASM international.

[46] Mattox, D.M., Handbook of physical vapor deposition (PVD) processing. William Andrew, 2010.

[47] Adapted from Pierson, H.O., Handbook of Chemical Vapor Deposition, Noyes Publications, 1992, Park Ridge.

[48] Xi, Y., Liu, D., Han, D., "Improvement of corrosion and wear resistances of AISI 420 martensitic stainless steel using plasma nitriding at low temperature." Surface and Coatings Technology, 2008, 202 (12): pp 2577-2583.

[49] Podgornik, B., et al. "Tribological properties of plasma nitrided and hard coated AISI 4140 steel." Wear, 2001, 249 (3): pp254-259.

[50] Podgornik, B., Jože, V., "Wear resistance of pulse plasma nitrided AISI 4140 and A355 steels." Materials Science and Engineering: A, 2001, 315 (1): pp 28-34.

[51] Wang, L., et al. "The wear and corrosion properties of stainless steel nitrided by low-pressure plasma-arc source ion nitriding at low temperatures." Surface and Coatings Technology, 2000 130 (2): pp 304-308.

[52] Corengia, P., et al. "Friction and rolling–sliding wear of DC-pulsed plasma nitrided AISI 410 martensitic stainless steel." Wear, 2006, 260 (4): pp 479-485.

[53] Wang, L., "Surface modification of AISI 304 austenitic stainless steel by plasma nitriding." Applied Surface Science, 2003, 211 (1): pp 308-314.

[54] Nie, X., et al. "Sliding wear behaviour of electrolytic plasma nitrided cast iron and steel." Surface and Coatings Technology, 2005, 200 (5): pp 1745-1750.

[55] Karakan, M., Akgün, A., and Ayhan, Ç., "Effect of process time on structural and tribological properties of ferritic plasma nitrocarburized AISI 4140 steel." Materials & design, 2004, 25 (4): pp 349-353.

[56] Karaoğlu, S., "Structural characterization and wear behavior of plasma-nitrided AISI 5140 low-alloy steel." Materials Characterization, 2002, 49 (4): pp 349-357.

[57] Leyland, A., et al. "Low temperature plasma diffusion treatment of stainless steels for improved wear resistance." Surface and Coatings Technology, 1993, 62 (1): pp 608-617.

[58] Sun, Y., Li, X., Bell, T., "Low temperature plasma carburising of austenitic stainless steels for improved wear and corrosion resistance." Surface Engineering (2013).

[59] PalDey, S. C. D. S., Deevi, S. C., "Single layer and multilayer wear resistant coatings of (Ti, Al) N: a review." Materials Science and Engineering: A, 2003, 342 (1): pp 58-79.

[60] Wilson, S., and Alpas, A.T., "TiN coating wear mechanisms in dry sliding contact against high speed steel." Surface and coatings Technology, 1998, 108: pp 369-376.

[61] Wilson, S., and Alpas, A.T., "Effect of temperature and sliding velocity on TiN coating wear." Surface and Coatings Technology, 1997 (94): pp 53-59.

[62] Huang, Z.P., Sun, Y., Bell, T., "Friction behaviour of TiN, CrN and (TiAl) N coatings." Wear, 1994, 173 (1): pp 13-20.

[63] Bull, S.J., et al. "High temperature mechanical properties of physical vapour deposited titanium nitride." Surface engineering (2013).

[64] Wilson, S., Alpas, A.T., "Effect of temperature on the sliding wear performance of Al alloys and Al matrix composites." Wear, 1996, 196 (1): pp 270-278.

[65] Kimura, A., et al. "Metastable $Ti_{1-x}Al_xN$ films with different Al content." Journal of materials science letters, 2000, 19 (7): pp 601-602.

[66] Zhou, M., et al. "Phase transition and properties of Ti–Al–N thin films prepared by rf-plasma assisted magnetron sputtering." Thin Solid Films, 1999, 339 (1): pp 203-208.

[67] Huang, C., Duh, J., "Deposition of (Ti, Al) N films on A2 tool steel by reactive rf magnetron sputtering." Surface and Coatings Technology, 1995, 71 (3): pp 259-266.

[68] Ikeda, T., Hiroshi S., "Phase formation and characterization of hard coatings in the TiAlN system prepared by the cathodic arc ion plating method." Thin Solid Films, 1991, 195 (1): pp 99-110.

[69] Tanaka, Y., et al. "Properties of $(Ti_{1-x}Al_x)$ N coatings for cutting tools prepared by the cathodic arc ion plating method." Journal of Vacuum Science & Technology A, 1992, 10 (4): pp 1749-1756.

[70] Musil, J., Hrubý, H., "Superhard nanocomposite Ti 1− x Al x N films prepared by magnetron sputtering." Thin Solid Films, 2000, 365 (1): pp 104-109.

[71] Jindal, P.C., Santhanam, A.T., Schleinkofer, U., Shuster, A.F., Performance of PVD TiN, TiCN, and TiAlN coated cemented carbide tools in turning. International Journey of Refractory Metals & Hard Materials, 1999 (17): pp 163-170

[72] Santhanam, A.T., Quinto, D.T., ASM Handbook, Surface Engineering 5, ASM International, Materials Park, OH (1994), pp 900-908

[73] Jindal, P. C., et al. "Performance of PVD TiN, TiCN, and TiAlN coated cemented carbide tools in turning." International Journal of Refractory Metals and Hard Materials, 1999, 17 (1): pp 163-170.

[74] Musameh, S.M., Jodeh, S.W., Tribological behavior of chromium nitride coating by unbalanced magnetron sputtering, Journey of Active and Passive Electronic Devices, 2007, 2: pp 93-103.

[75] Ehiasarian, A., Münz, W.D., Hultman, L., Helmersson, U., Petrov, I., High power pulsed magnetron sputtered CrNx films. Surface and Coating Technology, 2003, 163: pp 267-272.

[76] Polcar, T., Parreira, N.M.G., Novák, R., Friction and wear behaviour of CrN coating at temperatures up to 500 °C. Surface and Coating Technology, 2007, 201: pp 5228-5235.

[77] Barshilia, H.C., Selvakumar, N., Deepthi, B., Rajam, K., A comparative study of reactive direct current magnetron sputtered CrAlN and CrN coatings. Surface and Coatings Technology, 2006 (201): pp 2193–2201.

[78] Wu, Z., Qi, Z., Zhang, D., Wei, B., Wang, Z., Evaluating the influence of adding Nb on microstructure, hardness and oxidation resistance of CrN coating, Surface and Coatings Technology, 2016, 289: pp 45-51.

[79] Navinšek, B., Panjan, P., Milošev, I., Industrial applications of CrN (PVD) coatings, deposited at high and low temperatures, Surface and Coatings Technology, 1997, 97 (1-3): pp 182-191.

[80] Hones, P., Sanjinés, R., Lévy, F., Sputter deposited chromium nitride based ternary compounds for hard coatings, Thin Solid Films, 1998, 332 (1): pp 240-246.

[81] Hones, P., Consiglio, R., Randall, N., Lévy, F., Mechanical properties of hard chromium tungsten nitride coatings, Surface and Coatings Technology, 2000, 125 (1): pp 179-184.

[82] Cremer, R., Neuschütz, D., A combinatorial approach to the optimization of metastable multicomponent hard coatings, Surface and Coatings Technology, 2001, 146: pp 229-236.

[83] Wu, W., Wu, C., Xiao, B., Yang, T., Lin, S., Chen, P., Chang, C., Microstructure, mechanical and tribological properties of CrWN films deposited by DC magnetron sputtering, 2013, Vacuum, 87: pp 209-212

[84] INDEX FOR STAMPING DIES CAST MATERIALS TM.

[85] ASTM A681 - 08(2015) Standard Specification for Tool Steels Alloy.

[86] Chen, Y., Plasma electrolytic oxidation (PEO) coatings on a zirconium alloy for improved wear and corrosion resistance, 2010, Thesis, University of Windsor.

[87] Su, J., Nie, X., Impact-Sliding Wear Tests on Duplex-Treated Die Materials, Project: ASP360. Project No.: 11-2538-AMP.

# VITA AUCTORIS

NAME: Chen Zhao

PLACE OF BIRTH: Anhui, China

YEAR OF BIRTH: 1994

EDUCATION: Northwestern Polytechnical University, China

2010-2014, B.Sc

University of Windsor, Canada

2015-2017, M.A.Sc